# Numerical continuation and bifurcation for differential geometric PDEs

Alexander Meiners, Hannes Uecker

Institut für Mathematik, Universität Oldenburg, D26111 Oldenburg, alexander.meiners@uni-oldenburg.de, hannes.uecker@uni-oldenburg.de

May 3, 2024

**Abstract**

We describe some differential geometric bifurcation problems and their treatment in the MATLAB continuation and bifurcation toolbox `pde2path`. The continuation steps consist in solving the PDEs for the normal displacement of an immersed surface $X \subset \mathbb{R}^3$, with bifurcation detection and possible subsequent branch switching. The examples include minimal surfaces such as Enneper's surface and a Schwarz–P–family, some non–zero constant mean curvature surfaces such as liquid bridges, and some 4th order biomembrane models. In all of these we find interesting symmetry–breaking bifurcations. A few of these are (semi)analytically known and hence used as benchmarks.

# Contents

# 1 Introduction

Numerical continuation for partial differential equations (PDEs) yields the dependence of solutions on parameters, with special attention to bifurcation points, at which the local topological properties of the set of solutions change. These include fold points, where a branch folds back, and branch points, where different solution branches intersect. The list of toolboxes for numerical continuation of PDEs includes, e.g., `AUTO` [DCF+97] as a prototype package and role model, which in it's standard setup for PDEs is mainly aimed at 1D boundary value problems, Coco [DS13], `BifurcationKit.jl` [Vel20], and `pde2path` [UWR14, Uec21b, Uec24]. While all these packages in principle allow flexibility by delegating the PDE definition/discretization to the user, to the best of our knowledge they all rather focus on PDEs for functions $u : \Omega \times \Lambda \to \mathbb{R}^N$, where $\Omega \subset \mathbb{R}^d$ is a fixed domain, $d = 1, 2$, or 3, $N \in \mathbb{N}$, and $\Lambda \subset \mathbb{R}^p$ is a parameter domain, or on PDEs for time–dependent functions $u : I \times \Omega \times \Lambda \to \mathbb{R}^N$, $I \subset \mathbb{R}$, which then includes the continuation and bifurcation of time periodic orbits.

However, differential geometric PDEs in parametric form may deal directly with manifolds, e.g., surfaces in 2D, which are not graphs over a fixed domain. There are well established numerical methods for the discretization of such PDEs, for instance the surface FEM [DE13], but there seem to be few algorithms or packages which combine these with continuation and bifurcation. Two notable exceptions are the algorithm from [Bru18], and the `SurfaceEvolver` [Bra92], for which bifurcation aspects are for instance discussed in [Bra96]. Here we present geometric PDE bifurcation problems from demos for the `Xcont` extension of `pde2path`. More implementation details of `Xcont` and the demos are presented in the tutorial [MU24a], while here we focus on general principles and results, first for constant mean curvature surfaces, which are not necessarily graphs, and with the mean curvature, or the area or enclosed volume, as the primary bifurcation parameter, and second for some 4th order PDE biomembrane problems. See Fig.1 for a preview of the type of solutions we compute.

For $X$ a two dimensional surface immersed in $\mathbb{R}^3$, we for instance want to study the parameter dependent problem

$$H(\cdot) - H_0 = 0, \tag{1a}$$
$$V(X) - V_0 = 0, \tag{1b}$$

possibly with boundary conditions (BCs) in (1a), where $H(\cdot)$ is the mean curvature at each point of $X$, and $V(X)$ is the volume enclosed by $X$. The system (1) is obtained for minimizing the area $A(X)$ under the volume constraint $V(X) = V_0$, i.e., as the Euler–Lagrange equations for minimizing the energy

$$E(X) = A(X) + H_0(V(X) - V_0), \tag{2}$$

and $V_0 \in \mathbb{R}$ typically plays the role of an "external continuation parameter", while $H_0$, which for instance describes a spatially constant pressure difference for interfaces between fluids, is "free".

Following [Bru18], our setting for (1) and generalizations is as follows. Let $X_0$ be a surface satisfying (1) for some $V_0$ and $H_0$, and define a new surface via $X = X_0 + u\,N_0$, $u : X_0 \to \mathbb{R}$ with suitable boundary conditions, where $N_0 : X_0 \to \mathbb{S}^2$ is (a choice of) the unit normal vector field of $X_0$. Then (1) reads

$$G(u, \widetilde{H}) := H(X) - \widetilde{H} = 0, \quad \text{(with boundary conditions, if applicable)} \tag{3a}$$

which is a quasilinear elliptic PDE for $u$, coupled to the volume constraint

$$q(u) := V(X) - \widetilde{V} = 0. \tag{3b}$$

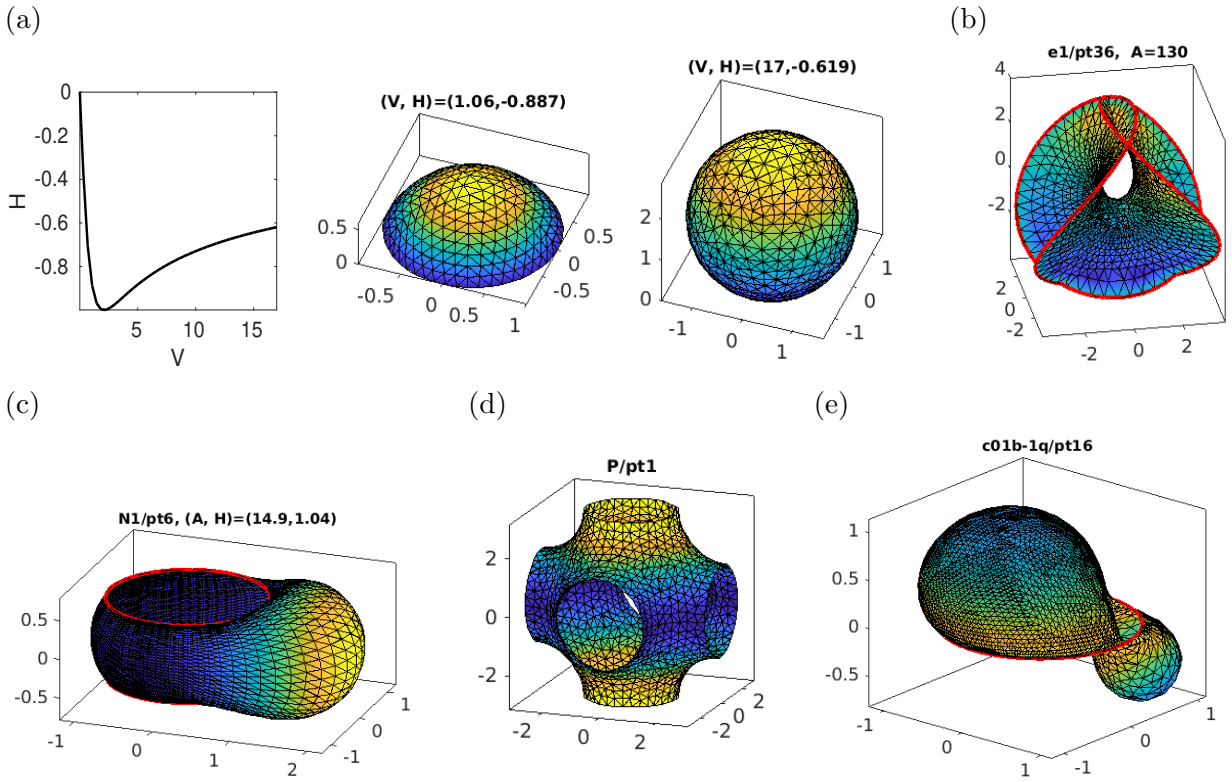


Figure 1: Preview of solutions (solution branches) we compute. (a) Mean curvature $H$ (negative since we choose the outer normal $N$) over volume $V$ for spherical caps, and sample solutions, §3.1. The colors indicate $u$ in the last continuation step, yellow>blue, and thus besides giving visual structure to $X$ indicate the "direction" of the continuation. (b) Enneper's minimal surface (a bounded part, with the boundary shown in red), §3.2. (c) A liquid bridge between two circles, with excess volume and hence after a symmetry breaking bifurcation, §3.3. (d) A Schwarz P surface, §3.4.1. (e) A Helfrich–type biomembrane cap after a symmetry breaking bifurcation. Samples (b)–(e) are each again from branches of solutions of the respective problems, see Figures 6, 7, 10, and 16.

Thus,

$$\text{after solving (3) for } u, \widetilde{H}, \widetilde{V} \text{ we can update } X_0 = X_0 + uN_0,\ H_0 = \widetilde{H}, V_0 = \widetilde{V}, \text{ and repeat.} \qquad (4)$$

More precisely, in (4) we use an arclength parameterization $s \mapsto (X(s), H_0(s))$ of solution branches, which allows to go around fold points (FPs) as solutions may go back and forth in parameter space. Moreover, during continuation we may detect and localize branch points (BPs), and subsequently return for branch switching to compute bifurcating branches.

We generally compute (approximate), e.g., the mean curvature $H$ from a surface FEM discretization of $X$, see §2.2. This can and usually must be combined with adaptive mesh refinement and coarsening as $X$ changes. Our methods can be applied to other geometric PDEs, also of higher order. For instance, for fourth order biomembrane models the analog of (3a) can be rewritten as a system of (2nd order) PDEs for a vector valued $u$, and the same ideas apply. Additionally, (1) and its generalizations often have to be combined with further constraints such as phase conditions to eliminate kernels due to symmetries.

The plan of the paper is as follows. In §2 we review some differential geometric background, and discretizations. In §3 and §4 we discuss the examples, and in §5 we give a summary, and an outlook on ongoing and future work. The appendix briefly reviews some basics of numerical continuation and bifurcation, and in particular how the `Xcont` addition extends the `pde2path` setup, and gives some technical details concerning mesh handling. Again we refer to [Uec21b] for general principles of nu-

merical continuation and bifurcation for PDEs, and a general description of `pde2path` and installation and first steps, and to [MU24a] for further implementation details of `Xcont` and all the demos. The rather large number of demos included in the download at [Uec24] and only partly explained here is aimed at showing versatility, and, more importantly, is due to our own needs for extensive testing, in particular of mesh handling strategies. See also [MU24b] for supplementary information (movies) on some of the rather complicated bifurcation diagrams we obtain. Table 1 summarizes acronyms and notation used throughout.

Table 1: Notations and acronyms; for given $X_0$, quantities of $X = X_0 + uN_0$ will also be considered as functions of $u$, e.g., $A(u) = A(X_0 + uN_0)$.

| | | | |
|---|---|---|---|
| $X$ | surface immersed in $\mathbb{R}^3$ | $N = N(X)$ | surface unit normal vector |
| $A$=$A(X)$=$A(u)$ | area of $X$, resp. of $X$=$X_0$+$uN_0$ | $V = V(X)$ | (algebraic) volume, e.g., (12) |
| $H = H(X)$ | mean curvature, e.g., (10) | $K = K(X)$ | Gaussian curvature |
| $G(u, \lambda) = 0$ | generic form of a PDE such as (3a), $\lambda$ as a generic parameter | ind$(X)$ | index, i.e., number of unstable eigenvalues of linearization |
| $L = \partial_u H(u)$ | Jacobi op. (with BCs) | $q(u, \lambda) = 0$ | generic constraint such as (3b) |
| BC | boundary condition | DBC/NBC | Dirichlet/Neumann BC |
| pBC | periodic BC | PC | phase condition |
| BP/FP | branch/fold point | CMC | constant mean curvature |
| TPS | triply periodic surface | TPMS | triply periodic minimal surface |

# 2 Background

## 2.1 Differential geometry

We briefly review some background from differential geometry, and recommend [Des04, Tap16, UY17] for further reading, among many others. Throughout, let $\Sigma$ be a connected compact orientable 2D manifold, with coordinates $x, y$, possibly with boundary $\partial\Sigma$, and for some $\alpha \in (0, 1)$ immersed by $X \in C^{2,\alpha}(\Sigma, \mathbb{R}^3)$. By pulling back the standard metric of $\mathbb{R}^3$ we obtain the first and second fundamental forms on $\Sigma$ expressed via $X$ as

$$g = \begin{pmatrix} g_{11} & g_{12} \\ g_{12} & g_{22} \end{pmatrix} = \begin{pmatrix} \|X_x\|^2 & \langle X_x, X_y\rangle \\ \langle X_x, X_y\rangle & \|X_y\|^2 \end{pmatrix}, \qquad h = \begin{pmatrix} h_{11} & h_{12} \\ h_{21} & h_{22} \end{pmatrix} = \begin{pmatrix} \langle X_{xx}, N\rangle & \langle X_{xy}, N\rangle \\ \langle X_{xy}, N\rangle & \langle X_{yy}, N\rangle \end{pmatrix}, \tag{5}$$

with unit normal $N$, which we consider as a field on $\Sigma$, or locally on $X$, which will be clear from the context. The mean curvature $H$ then is

$$H = \frac{1}{2} \frac{h_{11}g_{22} - 2h_{12}g_{12} + h_{22}g_{11}}{g_{11}g_{22} - g_{12}^2}, \tag{6}$$

which is the mean of the minimal and maximal normal curvatures $\kappa_1$ and $\kappa_2$, and

$$K = \kappa_1\kappa_2 \tag{7}$$

is the Gaussian curvature. The sign of $H$ depends on the orientation of $X$, i.e., on the choice of $N$. A sphere has positive $H$ iff $N$ is the inner normal. The Gaussian curvature does not depend on $N$ or any isometry of $\Sigma$ (Gauss's Theorema Egregium).

A generalization of the directional derivative of a function $f$ to vector fields or tensors is the covariant derivative $\nabla_Z$ for some vector field $Z$ on $X$. For a vector field $Y$, the covariant derivative in the $j$'th coordinate direction is defined as $\nabla_j Y_i := \partial_{x_j} Y_i + \Gamma^i_{jk} Y_k$, and for a 1-form $\omega$ we have

$\nabla_j \omega_i := \partial_{x_j}\omega_i - \Gamma^i_{jk}\omega_k$, with the Christoffel symbols $\Gamma^i_{jk} = \frac{1}{2}g^{il}(\partial_{x_j}g_{kl} + \partial_{x_k}g_{jl} - \partial_{x_l}g_{jk})$, where $g^{ij}$ are the entries of $g^{-1}$ and we use Einstein's summation convention, i.e., summation over repeated indices. The covariant derivative is linear in the first argument, giving a general definition of $\nabla_Z Y$ with some vector field $Z$, and if $f$ is a function on $X$, then

$$\nabla_Z f = \langle g\nabla f, Z\rangle_{\mathbb{R}^2}. \tag{8}$$

Throughout we are dealing with surfaces (2D manifolds immersed into $\mathbb{R}^3$), hence the gradient $\nabla$ is the *surface gradient*, i.e., the usual gradient $\nabla_{\mathbb{R}^d}$ in $\mathbb{R}^3$ projected onto the tangent space,

$$\nabla f = \nabla_{\mathbb{R}^3} f - \langle \nabla_{\mathbb{R}^3} f, N\rangle\, N, \tag{9}$$

which later will be needed to (formulate and) implement phase conditions, and, e.g., Neumann type BCs. This also gives the *Laplace Beltrami operator* via

$$\Delta f = g^{ij}\nabla_i \nabla_j f,$$

which then also applies to general tensors. The Gauss–Weingarten relation $\partial_{x_i}\partial_{x_j}X = \Gamma^k_{ij}\partial_{x_k}X + h_{ij}N$ yields

$$\Delta X = g^{ij}\nabla_i\nabla_j X = g^{ij}\left(\partial_{x_i}\partial_{x_j}X - \Gamma^i_{jk}\partial_{x_k}X\right) = g^{ij}h_{ij}N = 2HN = 2\vec{H},$$

where $\vec{H}(\cdot)$ is called the mean curvature vector (field), and

$$H(\cdot) = \frac{1}{2}\langle \Delta X(\cdot), N(\cdot)\rangle. \tag{10}$$

The area of $X$ is

$$A(X) = \int_X \mathrm{d}S, \tag{11}$$

and, based on Gauss's divergence theorem, the (algebraic) volume is

$$V(X) = \frac{1}{3}\int_X \langle X, N\rangle\ \mathrm{d}S. \tag{12}$$

If $X$ is a closed embedded manifold bounding $\Omega \subset \mathbb{R}^3$, i.e., $\partial\Omega = X$, and $N$ the outer normal, then $V(X) = |\Omega|$ is the physical volume. If $X$ is not closed, then we typically need to add a third of the flux of $\vec{x}$ through the open ends to $V(X)$ (see the examples below).

We denote the set of all immersed surfaces with the same boundary $\gamma$ by

$$\mathcal{N}_\gamma = \{X : X \text{ is an immersed surface and } \partial X = \gamma\}. \tag{13}$$

The following lemma states that all immersions $Y \in \mathcal{N}_\gamma$ close to $X$ are graphs over $X$ determined by a function $u$ as $Y = X + uN$, which justifies our numerical approach (4). The condition that $Y$ has the same boundary as $X$ in general cannot be dropped, as obviously motions of $\partial X$ tangential to $X$ cannot be captured in the form $X + uN$.

**Lemma 2.1** *[KPP17]. For $X \in C^{2,\alpha}(\Sigma, \mathbb{R}^3)$ with boundary $\partial X = \gamma$ there exists a neighborhood $U \subset C^{2,\alpha}(\Sigma, \mathbb{R}^3)$ of $X$ such that for all $Y \in U \cap \mathcal{N}_\gamma$ there exists a diffeomorphism $\phi : \Sigma \to \Sigma$ and a*

*function* $u \in C^{2,\alpha}(\Sigma)$ *such that*

$$Y \circ \phi = X + u\,N. \tag{14}$$

Assume that a CMC surface $X_0$ with boundary $\partial X_0{=}\gamma$ and volume $V(X_0){=}V_0$ belongs to a family of CMC surfaces $X_t$, $t \in (-\varepsilon, \varepsilon)$ for some $\varepsilon > 0$. For example, the spherical caps $S_t$ from Fig. 1(a) with the boundary $\gamma = \{(x, y, 0) \in \mathbb{R}^3 : x^2 + y^2 = 1\}$ are a family of CMC immersions fully described by the height $t \in \mathbb{R}$. By Lemma 2.1, the parameter $t$ uniquely defines $u$ in a small neighborhood of $X_0$, i.e., $X_t = X_0 + u\,N$, and the system of equations for $u$ reads

$$H(u) - H_0 = 0, \tag{15}$$

for some $H_0 \in \mathbb{R}$, where we abbreviate $H(u) = H(X + u\,N)$, etc. If we consider variational vector fields at $X_0$ in the form $\psi = \partial_t X_t|_{t=0} = uN$, and additionally assume that $X_t \in \mathcal{N}_\gamma$, then necessarily

$$u|_{\partial X} = 0, \text{ (Dirichlet boundary conditions, DBCs).} \tag{16}$$

Such an $X_t$ is called an *admissible variation* in [Lóp13, §2.1], and we have the following results on derivatives of $A$ and $V$.

**Lemma 2.2** *[Lóp13, §2.1] For an admissible one parameter variation* $X_t$ *of* $X \in C^{2,\alpha}(\Sigma)$ *and variational vector fields* $\psi = \partial_t X\big|_{t=0} = uN$*, the functions* $t \mapsto A(t) = A(X_t)$ *and* $t \mapsto V(t) = V(X_t)$ *are smooth, and*

$$V'(0) = \int_{X_0} u\,\mathrm{d}S, \quad A'(0) = -2\int_{X_0} H_0 u\,\mathrm{d}S, \quad A''(0) = -\int_{X_0} (\Delta u + \|\mathcal{S}_0\|^2 u)u\,\mathrm{d}S, \tag{17}$$

*where* $\|\mathcal{S}_0\|^2 = 4H_0^2 - 2K_0$ *with the Gaussian curvature* $K_0$*. Thus*

$$\frac{\mathrm{d}}{\mathrm{d}t} H(X_t)\Big|_{t=0} = -\frac{1}{2}(\Delta u + \|\mathcal{S}_0\|^2 u), \tag{18}$$

*and the directional derivative* (18) *is given by the self-adjoint Fredholm operator* $\mathcal{L}$ *on* $L^2(X_0)$ *with*

$$\mathcal{L} = \partial_u H(0) = -\frac{1}{2}(\Delta + \|\mathcal{S}_0\|^2), \quad \textit{with DBCs.} \tag{19}$$

**Remark 2.3** a) The operator in (19) without BCs is called *Jacobi operator*, and a nontrivial kernel function is called a *Jacobi field* on $X = X_0$. An immersion $X$ with a Jacobi field satisfying the BCs is called *degenerate*. The Fredholm property allows the use of the Crandall-Rabinowitz bifurcation result [CR71]: Given a $C^1$ branch $(t_0{-}\varepsilon, t_0{+}\varepsilon) \ni t \mapsto X_t$, if $X_t$ is non–degenerate for $t \in (t_0{-}\varepsilon, t_0){\cup}(t_0, t_0{+}\varepsilon)$, and if at $t_0$ a *simple* eigenvalue $t \mapsto \mu_0(t)$ crosses transversally, i.e., $\mu(t_0) = 0$, $\mu_0'(t_0) \neq 0$, then a branch $\widetilde{X}_t$ bifurcates at $t_0$.

See also [KPP17] for a formulation via Morse indices $\mathrm{ind}(X_t)$=number of negative eigenvalues of $\mathcal{L}$, counted with multiplicity, used to find bifurcation points in families of nodoids, which we shall numerically corroborate in §3.3.2. An "equivariant version" (factoring out continuous symmetries) can be found in [KPS18, Theorem 5.4], applied to bifurcations of triply periodic minimal surfaces, for which linearizations always have a trivial 5–dimensional kernel due to translations and rotations, see §3.4 for numerical illustration. See also [GS02, Hoy06, Kie12] and [Uec21b, Chapters 2 and 3] for general discussion of Crandall–Rabinowitz type results, and of Krasnoselski type results (odd multiplicity of critical eigenvalues, based on degree theory), including equivariant versions. ⌋

## 2.2 Discrete differential geometry FEM operators

We recall a few discrete differential geometry operators from [MDSB03, Jac13], and shall use implementations of them from the `gptoolbox` [Jac24]. Given a triangulation

$$\texttt{X} \in \mathbb{R}^{n_p \times 3} \text{ (point coordinates) and } \texttt{tri} \in \mathbb{R}^{n_t \times 3} \text{ (triangle corner indices)} \tag{20}$$

of $X$, and the piecewise linear element "hat" functions $\phi_i : X \to \mathbb{R}$, $\phi_i(X_j) = \delta_{ij}$, we have

$$\int \nabla\phi_i \nabla\phi_j \,\mathrm{d}S = \frac{1}{2}(\cot\alpha_{ij} + \cot\beta_{ij}) =: L_{ij}, \tag{21}$$

where $\alpha_{ij}$ and $\beta_{ij}$ are the angles opposite the edge $e_{ij}$ from point $X_i$ to point $X_j$. For $u : X \to \mathbb{R}$, $u = \sum_{i=1}^{n_p} u_i\phi_i$, this yields the FEM stiffness matrix $L$ such that $Lu$ corresponds to the Laplace–Beltrami operator $-\Delta u$ weighted by the mass matrix $M$. In [MDSB03] it is explained that for geometric problems, instead of the full mass matrix $M_{\text{full}}$ with

$$M_{\text{full},ij} = \int \phi_i\phi_j \,\mathrm{d}S, \tag{22}$$

the Voronoi mass matrix

$$M = \operatorname{diag}(A_1, \ldots, A_{n_p}), \tag{23}$$

should be expected to give better approximations. Here, $A_i = \sum_{j=1}^{n_i} A_m(T_j)$ is the area of the Voronoi region at node $i$, where $T_j$, $j = 1, \ldots, n_i$ are the adjacent triangles, and $A_m(T)$ is a "mixed" area: For non–obtuse $T$, $A_m(T)$ is the area of the rhomb with corners in $X_i$, in the midpoints of the edges adjacent to $X_i$, and in the circumcenter of $T$, while for obtuse $T$ we let $A_m(T) := |T|/2$ if the angle at $X_i$ is obtuse, and $A_m(T) := |T|/4$ else. Altogether, this yields the approximation

$$-\Delta u = M^{-1}Lu, \tag{24}$$

where $M$ from (23) is diagonal, and $L$ and $M$ are evaluated efficiently via `cotmatrix` and `massmatrix` from the `gptoolbox`.

However, as we always consider our problems such as (3) in weak form, we let $\texttt{H} = \frac{1}{2}\langle LX, N\rangle$, with vertex normals $N$, and the weak form of, e.g., $H - H_0{=}0$ then is

$$\langle LX, N\rangle - 2MH_0 = 0, \tag{25}$$

again with Voronoi $M$. Alternatively, we use `[k,H,K,M]=discrete_curvatures(X,tri)`, where `K` and $\texttt{k} = (k_1, k_2)$ are the (weighted, i.e., weak) discrete Gaussian and principal curvatures per vertex; these are computed from a discrete version of the Gauss–Bonnet theorem.[1] Namely

$$\texttt{K}(X_i) = 2\pi - \sum_{j=1}^{n_i} \theta_j, \quad (\text{and } k_1 = H + \sqrt{D} \text{ and } k_2 = H - \sqrt{D}), \tag{26}$$

where the $\theta_j$ are the angles at $X_i$, and where the discriminant $D = H^2 - K$ (which is non-negative

[1] On a manifold $X$ with boundary $\partial X$ we have $\int_X K\,\mathrm{d}S + \int_{\partial X} \kappa_g\,\mathrm{d}s = 2\pi\chi(X)$ where $\chi(X)$ is the Euler characteristic of $X$, and $\kappa_g$ is the geodesic curvature of $\partial X$. This will play an important role for the biomembranes in §4. The discrete formula (26) is used at interior points of $X$, while at boundary points $X_i$ it is modified to $K(X_i) - \pi$.

in the continuous case) in the discrete case is set to 0 if negative. An approximations of $K$ is then obtained (cheaply, since $M$ is diagonal) from

$$K = M^{-1}\mathtt{K}. \tag{27}$$

For notions of convergence of discrete differential geometry objects and operators we refer to [War08], which considers approximations of a smooth manifold $X$ by shape regular triangulations $X_h$ in the sense of Hausdorff distance $\operatorname{dist}(X_h, X) \to 0$ as $h \to 0$. Here and in the following $h = \max_{T\in\mathtt{tri}} h(T)$, where $h(T)$ means the maximal edge length of triangle $T$, and shape regular means that the mesh distortions

$$\delta_{\text{mesh}} := \max_{T\in\mathtt{tri}} (h(T)/r(T)) \quad \text{(max edge-length over in–radius)}, \tag{28}$$

are bounded.[2] Then, the following convergences are equivalent:

$$\begin{array}{ll} \text{(a)} & \text{normals } \|N - N_h\|_\infty \to 0, \\ \text{(b)} & \text{volumes (area) } \|\,\mathrm{d}S - \mathrm{d}S_h\|_\infty \to 0, \\ \text{(c)} & \text{Laplace-Beltrami operators } \|\Delta - \Delta_h\|_{\text{op}} \to 0, \end{array} \tag{29}$$

where $\|\cdot\|_{\text{op}}$ is the norm in $L(H_0^1(X), H^{-1}(X))$ and $\mathrm{d}S_h$ and $\Delta_h$ in (29) are to be understood in a metric pullback sense. A fourth notion of convergence equivalent to those in (29) and in fact used for the proof of the equivalence in (29) is metric convergence (suitably defined). In particular, in general the discrete mean curvature $H_h$ obtained from $H_h(X_h) = \frac{1}{2}\langle \Delta_h X_h, N_h\rangle$ only converges as a functional to $H(X)$, not as function. A famous counterexample that (hence) none of the convergences from (29) follows from $\operatorname{dist}(X_h, X) \to 0$ alone is the lantern of Schwarz. Nevertheless, while numerical experiments in [Xu04] show that a variety of natural schemes for $\Delta$ in general do not converge, [Xu04, Theorem 2.1] states that with Voronoi $M$ and at valence six nodes (six neighbors)

$$M^{-1}L = \Delta + \mathcal{O}(h^2); \tag{30}$$

see also [XX09] for function space convergence as $h \to 0$ of various schemes for $H_h$ and $K_h$.

In Fig.2 (and Fig. 3) we give an illustration of the (function space) error and convergence behavior of our discrete $H = \frac{1}{2}M^{-1}\langle LX, N\rangle$ based on (24), and of $K$ from (27), for discretizations of the unit sphere obtained from subdivision and projection. Here $N$=outer normal, hence $H = -1$ and $K = 1$ are the exact values, and the two left columns indicate the convergence for $H$, but also that the node valence plays a role on these otherwise very regular meshes.[3] However, the last column shows that using $M_{\text{full}}$ in this example, i.e., $H_{\text{full}} = \frac{1}{2}{M_{\text{full}}}^{-1}\langle LX, N\rangle$ gives a significant error (and similarly in $K$), and in fact no convergence at the valence 5 nodes.

Figure 3(a) shows the pointwise convergence of $H$ and $K$ (away from the boundary) for a hemisphere discretized by subdivision and projection with $j$=2, …, 5 steps, see `geomtut/hemispconv/` for the MATLAB source. Here, "$\|H+1\|_\infty, \alpha = -1.03$" in the legend means $\|H+1\|_\infty \sim Cn^\alpha$ with $\alpha$ the best linear fit for the log–log plot. Since $n \sim h^{-2}$, (a) shows that here (30) also holds at the valence 5 nodes, and that also for $K$ we get the same convergence. In (b) we show the data for the $L^2$ norm, in which $H_{\text{full}}$ and $K_{\text{full}}$ also converge (because the "density" of valence 5 nodes goes to zero,

[2] $\delta_{\text{mesh}}$ will also be one of our criteria for mesh adaptation in the numerics; for an equilateral triangle (best case) $\delta_{\text{mesh}} = 2\sqrt{3} \approx 3.46$, and for a right angled isoceles triangle $\delta_{\text{mesh}} \approx 4.83$. As a rule of thump, meshes with $\delta_{\text{mesh}} \le 10$ have little distortion, and $\delta_{\text{mesh}} \le 50$ is still OK. See also [She02] for a very useful discussion of mesh quality (in the planar setting, and in 3D).

[3] Euler's polyhedron formula yields that triangulations with all nodes of valence 6 do not exist, see, e.g., [BF67].

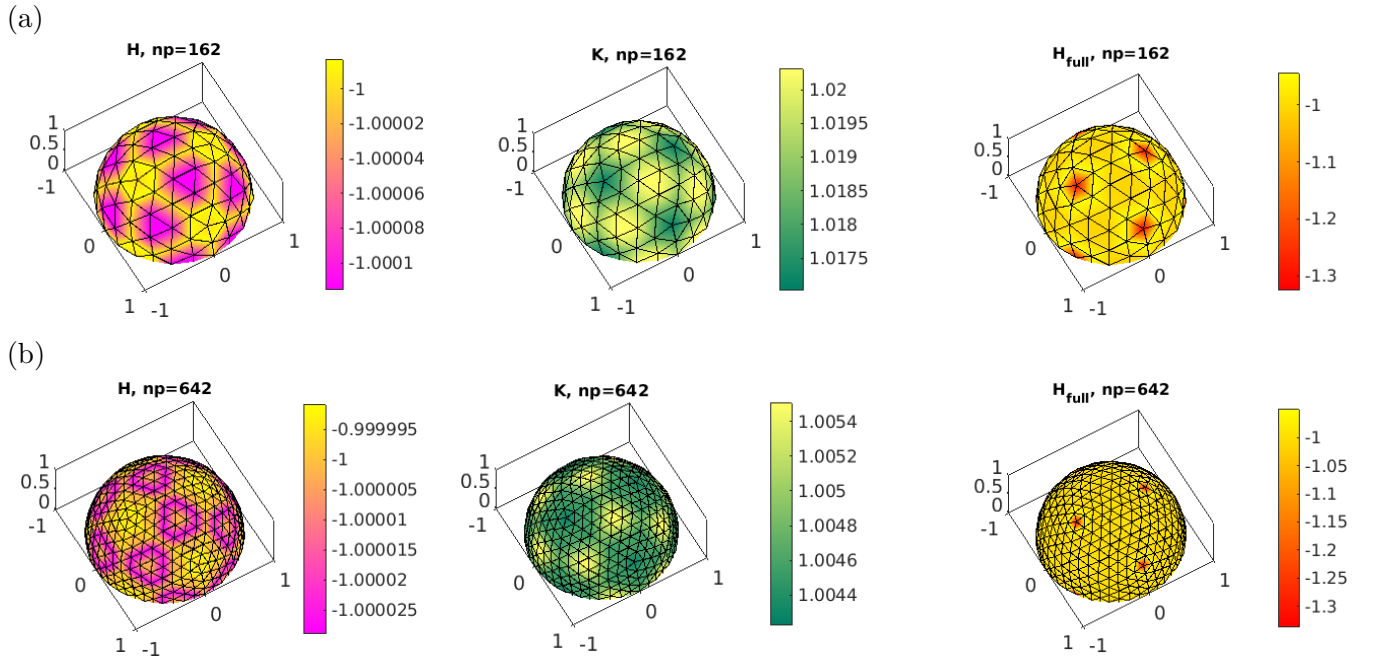


Figure 2: Discrete $H$ (and $K$) on (coarse) meshes of the unit sphere (plots cropped). Two left columns: Convergence for $H = -\frac{1}{2}M^{-1}\langle LX, N\rangle$ and $K = M^{-1}\mathtt{K}$ with Voronoi $M$. Right column: No convergence for $H$ (and similar for $K$) at valence 5 nodes when using $M_{\text{full}}$.

see MATLAB sources for plots), but with much slower rates than $H$ and $K$.

Finally, (c) shows a different experiment: after initialization with the hemispheres from (a), we solve the discretized problem $H + 1 = 0$ with DBCs $\partial X = S^1$, i.e., $u = 0$ for the nodes associated to $\partial X$, and plot the deviation of $X$ from the spherical shape. The convergence rate for $|X| - 1$ is approximately $n^{-5/3}$, both for $X$ and $X_{\text{full}}$ (obtained with $M_{\text{full}}$), and in both $\|\cdot\|_\infty$ and in $\|\cdot\|_2$. Thus, while $H_{\text{full}}$ is in general not accurate, here the solution $X_{\text{full}}$ is. In any case, in the following we always use the Voronoi mass matrix $M$ and generally recommend this. See also Example A.2 for another convergence experiment, where we also explain different options for mesh refinement, and where we display some lingering effects of the valence of nodes on solution accuracy.

# 3 Second order examples

Our examples are meant to illustrate a variety of differential geometric bifurcation problems, in particular with different BCs. We start with spherical caps as an introductory example, and then consider classical minimal and CMC surfaces, for instance the Enneper and Schwarz–P surfaces, and so called nodoids (including physically relevant liquid bridges). In §4 we consider 4th order problems obtained from the Helfrich functional.

For the basic setup of numerical continuation and bifurcation in the `Xcont` setting we again refer to §A, based on the general principles explained in [Uec21b], and for more implementation details of the demos to [MU24a]; here we mostly focus on results, and highlight only some of the numerical issues associated with the demos.

## 3.1 Spherical caps

We start with the continuation in volume $V$ of spherical caps over the unit circle $\gamma$ in the $x$–$y$ plane, as previewed in Fig. 1(a). It is known [ALP99],[KPP15, §2.6] that no bifurcations occur, and hence this only serves as an introductory toy model. The BCs are $\partial X = \gamma = \{(x, y, 0) \in \mathbb{R}^3 : x^2 + y^2 = 1\}$, which since they hold for the initial unit disk translate into $u|_\gamma = 0$. Thus, our complete problem

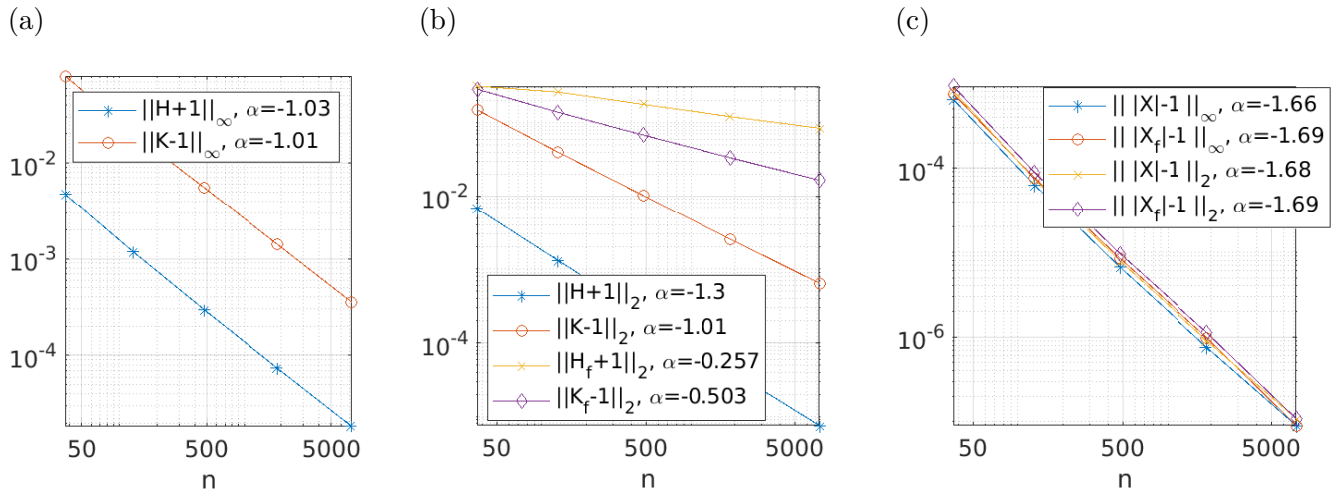


Figure 3: (a,b) Convergence rates for $H$ and $K$ on discretized hemipsheres. (c) Convergence rates for the spherical deviation $|X| - 1$ of solutions of $H + 1 = 0$.

reads

$$G(u) := H(u) - H_0 = 0, \quad u|_{\partial X} = 0, \quad q(u) := V(u) - V_0 = 0, \tag{31}$$

with external parameters $(V_0, H_0)$. Listing 1 exemplarily shows the implementation of the PDE $H(u) - H_0 = 0$, and again we refer to §A for general principles, and to [MU24a] for more details on all of the altogether five basic function files (initialization `scinit.m`, PDE-rhs `sGsc.m`, Jacobian `scjac.m`, MCF right hand side `mcf.m`, branch output `cmcbra.m`) needed to run (31) in the script files `cmds1.m, cmds2.m` and `cmds3.m`. Nevertheless, while we refrain from displaying further m–files, we keep the references to the scripts as we recommend to run these in parallel to this document.

```
function r=sGsc(p,u) % spherical cap PDE (more generally: CMC with DBCs)
par=u(p.nu+1:end); H0=par(1); u=u(1:p.np); % split into u and parameters
N0=getN(p,p.X); X=p.X+u.*N0; N=getN(p,X); % normal, new X, new normal
M=getM(p,X); LB=cotmatrix(X,p.tri);  % mass matrix and Laplace-Beltrami
r=-0.5*dot(LB*X,N,2)+M*(H0*ones(p.np,1)); % rhs-PDE, i.e., -H(X)+H0=0
r(p.idx)=u(p.idx);    % Dirichlet BCs
```

Listing 1: `geomtut/spcap1/sGsc.m`, implementing the PDE $H(X) - H_0 = 0$, to be prepared by `scinit.m`.

Basic results on the continuation of the initial disk (with $V = 0$ and $A = \pi$) in $V$ are already given in Fig. 1(a); $H$ (negative since we use the outer normal) reaches the minimum $H = -1$ at $V \approx \pi$ corresponding to a hemisphere, and as $V$ increases we need mesh adaptation. We refer to §A.3 for general principles for this, and in Fig. 4 illustrate some options.[4] The black line `capr1` in (a) corresponds to refinement each 15th step, where we use the triangle areas on $X$ as selector for the triangles to refine, and "refinement factor" $\sigma = 0.3$ (fraction of triangles marked for refinement). Here we only bisect the longest edge of a selected triangle, in short "refine–long", and the fraction of refined triangles is between $\sigma$ and $2\sigma$.

For `capr3` (red) we refine when the "error" $e(X)$ exceeds 0.04, where $e(X)$ is also used for plotting and defined as follows: For given $V$ we compute the (exact) $H_{\text{ex}}(V)$ of the associated (exact) spherical

[4]Fig. 4(a,b) shows essentially verbatim output from `plotbra` in `cmds2.m`, where the dots and numbers indicate the continuation step, subsequently used also in the sample plots as in (c). This also holds for all subsequent plots, and the only "manual adjustments" are the occasional repositioning of the numbers at the arrows by drag and drop.

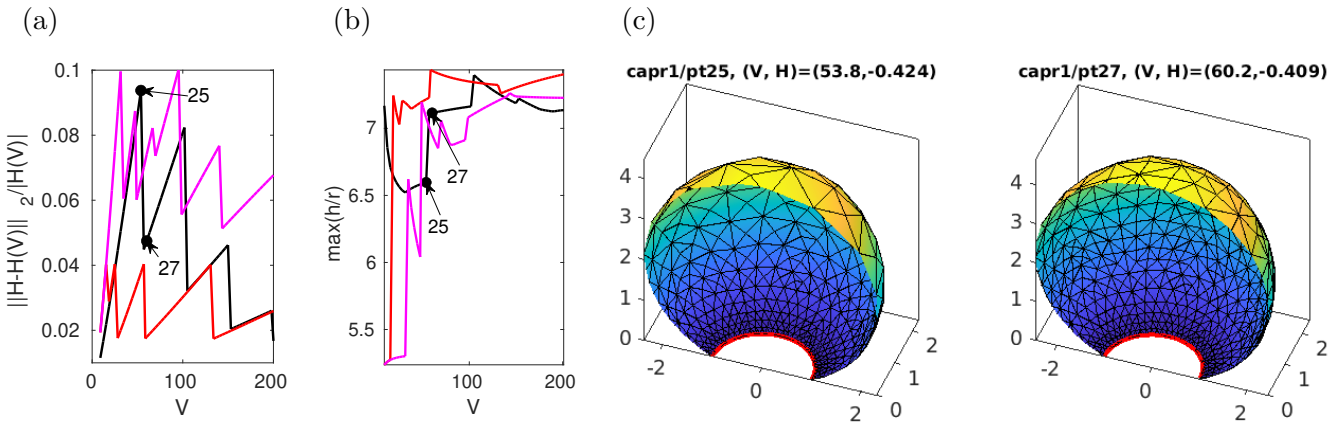


Figure 4: Results from `spcap1/cmds2.m`. (a) Error $e(X) := \|H - H(V)\|_2/|H(V)|$ for refinement each 15th step (`capr1`, black) (starting at step 10), when $e(X) >$ `p.nc.errtol` $= 0.05$, using `p.fuha.ufu=@refufu` (`capr3`, red), and when $\max(A) > 0.3$ using `p.fuha.ufu=@refufumaxA` with $\sigma = 0.3$ (`capr4`, magenta). At $V = 200$, $n_p = 1452$ on `capr1`, $n_p = 1486$ on `capr3`, and $n_p = 636$ on `capr4`. (b) Mesh distortion $\delta_{\text{mesh}} = \max(h/r)$ (edge-length over in–radius). (c) Illustration of meshes before/after refinement at pt25; plots cropped at $y = 0$ for better visibility of the meshes, and the boundary at $z = 0$ marked in red.

cap as $H_{\text{ex}}(V) = -\dfrac{\pi^{1/3}(3V+s-\pi^{2/3})(s-3V)^{1/3}}{s(3V+s)^{1/3}}$, $s = \sqrt{9V^2+\pi^2}$. We then define the "relative $L^2$ error"

$$e(X) = \|H(X) - H_{\text{ex}}(V)\|_{L^2(X)}/|H_{\text{ex}}(V)|, \tag{32}$$

and put $e(X)$ on the branch in the modified local copy `cmcbra.m` of the standard (library) `cmcbra.m`. $e(X)$ can then be plotted like any other output variable, and, moreover, can be used (without recomputing) in `p.fuha.ufu` (user function), which is called after each successful continuation step. The default (library) setting `p.fuha.ufu=@stanufu` essentially only gives printout, and to switch on the adaptive meshing we rename and modify a local copy as `refufu.m`, and set `p.fuha.ufu=@refufu`.

Another "natural" alternative is to refine when

$$a_{\max} = \max(a_1, \ldots, a_{nt}) > \texttt{p.maxA}, \tag{33}$$

i.e., when the maximum area of the `nt` triangles exceeds a chosen bound. This is *not* an error estimator in any sense (as a plane can be discretized by arbitrary large triangles), but an ad hoc criterion, with typically an ad hoc choice of `p.maxA`. In detail, if $\max A >$`p.maxA`, then `refufumaxA.m` bisects all triangles with $A > (1-\sigma)$`p.maxA`. With `p.maxA`$=0.3$ and $\sigma=0.2$ this yields the magenta line in Fig.4(a). In (b) we plot the mesh distortion $\delta_{\text{mesh}} = \max_{\text{triangles}}(h/r)$, cf. (28).

The samples in Fig.4(c) illustrate a refinement step on the black branch, yielding a reasonable mesh also at large $V$. However, this naturally depends on the choice of steps between refinements (and on the refinement fraction $\sigma$ and continuation stepsize `ds`). For the red line in Fig. 4(a), the refinement when the error $e(X)$ exceeds the chosen bound `p.nc.errbound` is more genuinely adaptive, and this similarly holds for `capr4` based on (33). (b) shows that the long–refinement generally yields a (mild) increase of the mesh distortion $\delta_{\text{mesh}}$, but overall the mesh–quality stays very good. In summary, with any of the above strategies we can robustly, accurately and quickly continue to arbitrary large $V$, i.e., arbitrary large cap radius $R$, where $H = 1/R$ asymptotes to $H = 0$.

In `cmds3.m` and Fig. 5 we *decrease* $V$ from $V \approx 150$ (running the branch `capr1` from Fig. 4 backwards), and test mean curvature flow (MCF, see Remark 3.1) from a spherical cap at $V \approx 15$. For both, because the shrinking of the caps gives mesh distortions, the main issue is that we now need to alternate continuation/flow and mesh–*coarsening*. For the continuation we give two options: similar

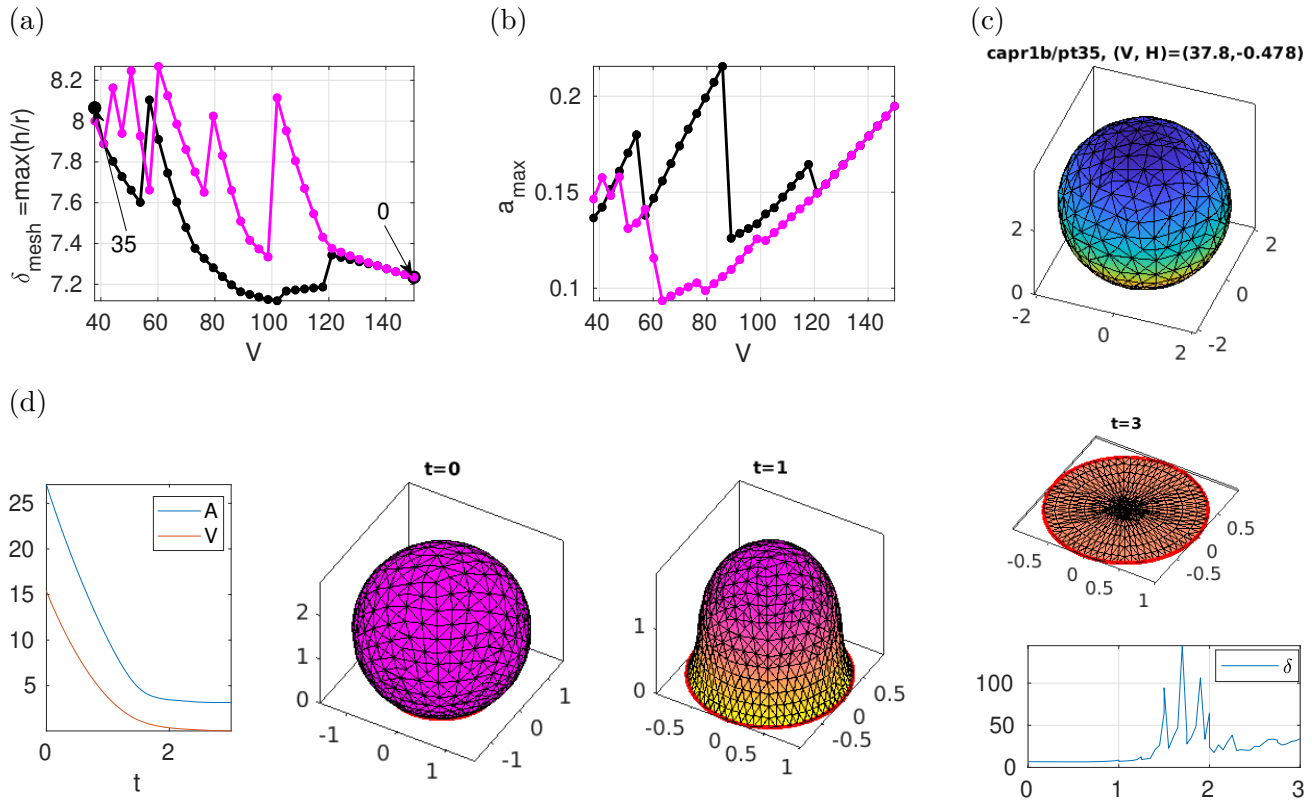


Figure 5: Results from `spcap1/cmds3.m`. (a)-(c) continuation backwards in $V$ from $V{\approx}150$ ($n_p$=1452); coarsening each 5th step (`capr1b`, black, $n_p$=644 at $V$=40) vs coarsening when $\delta_{\text{mesh}} > 8$ (magenta, $n_p$=650 at $V$=40)). (d) MCF from the spherical cap at $V{\approx}15$. time series of $A$ and $V$, sample plots, and time series of $\delta_{\text{mesh}}$ (last plot). Coarsening at times $t = 0.25j$, altogether from $n_p = 773$ at $t = 0$ to $n_p = 450$ at $t = 3$.

to the refinement for increasing $V$ in Fig. 4, we either coarsen after a fixed number of steps (black branch), or when $\delta_{\text{mesh}}{>}8$ (magenta branch). Both here work efficiently only until $V{\approx}35$, after which new parameters for the coarsening should be chosen. For the MCF in (d) we similarly coarsen after a given number of time steps. With this we can flow back to the disk, essentially reached at $t$=3, but the last plot in (d) shows that along the way we have strongly distorted meshes, which are somewhat repaired in the coarsening steps, and the final distortion with $\delta_{\text{mesh}}{\approx}30$ is not small but OK.

**Remark 3.1** a) A time $t$ dependent 2D manifold $X(t) \subset \mathbb{R}^3$ deforms by mean curvature flow (MCF) if (choosing the inner normal for $N$)

$$\dot{X} = -H(X)N. \tag{34}$$

This is the $L^2$ gradient flow for the area functional $A(X)$, and can be considered as a quasilinear parabolic PDE, at least on short times. For closed and compact $X$ there always is finite time blowup (for convex $X$ by shrinking to a "spherical point"), and we refer to [Man11] for an introduction to this huge field, which inter alia heavily relies on maximum (comparison) principles.

Solutions of problems of type (1), i.e., $H(\cdot) - H_0 = 0$, $V(X) - V_0 = 0$, give critical points of the volume preserving mean curvature flow

$$\dot{X} = -(H(X) - \overline{H})N, \quad \overline{H} = \frac{1}{A(X)} \int_X H \, \mathrm{d}S, \tag{35}$$

and for closed $X$ conserves the enclosed volume $V(X)$. For non–closed $X$ one typically studies Neumann type BCs on "support planes", see, e.g., [Har13], and [MU24a, §A] for numerical examples,

and in most cases the analysis is done near axisymmetric states such as spheres, spherical caps, and cylinders. In general, the existence and regularity theory for (35) is less well understood than for (34) due to the lack of general maximum principles for (35).

Our notion of stability of solutions of (1) (indicated by thick lines in bifurcation diagrams, while branches of unstable solutions are drawn as thinner lines) refers to (35) if we have an active volume constraint such as (3b), and to (34) if not.

b) We use basic methods to numerically integrate (34) and (35) by explicit Euler stepping, i.e.,

$$X_{n+1} = X_n - \mathtt{dt} H(X_n) N(X_n), \tag{36}$$

for (34) with a sufficiently small temporal stepsize `dt`, but so far without stepsize control, see c). As indicated in Fig.5(d), this often has to be combined with mesh adaptation, and in this case $A$ does not necessarily decrease monotonously for MCF. In summary, (36) is not particularly efficient or accurate, but can for instance be used to generate initial guesses for the continuation of steady states of (1), see also §3.2 for an example. We refer to [BNP10, BGN20, BGNZ22] for more sophisticated numerical algorithms for geometric flows including (34) and (35), and detailed discussion.

c) The performance of the MCF as in Fig. 5, based on (36), depends on the choice of parameters, i.e., step size `dt`, number $n_{\mathrm{f}}$ of steps before coarsening, and coarsening factor $\sigma$. With too weak coarsening (large $n_{\mathrm{f}}$, or small $\sigma$), triangles may degenerate. Too aggressive coarsening (large $\sigma$) may lead to wrong identification of boundary edges. Altogether, at this point we must recommend trial and error. ⌋

## 3.2 Enneper's surfaces

Plateau's problem consists in finding soap films $X$ spanning a (Jordan) curve (a wire) $\gamma$ in $\mathbb{R}^3$, and minimizing area $A$. Mathematically, we seek a *minimal* surface $X$, i.e., $H(X) \equiv 0$, with $\partial X = \gamma$. Such problems have a long history, and already Plateau discussed non–uniqueness and bifurcation issues, called "limits of stability" in [Pla73].

Enneper's surface is a classical minimal surface. Bounded parts of it can be parameterized by[5]

$$X_E = X_E(r,\vartheta) = \begin{pmatrix} r\cos(\vartheta) - \frac{r^3}{3}\cos(3\vartheta) \\ -r\sin(\vartheta) - \frac{r^3}{3}\sin(3\vartheta) \\ r^2\cos(2\vartheta) \end{pmatrix}, \quad (r,\vartheta) \in D_\alpha = [0,\alpha)\times[0,2\pi). \tag{37}$$

We start with some basic facts, see [BT84] and the references therein. For $\alpha \le 1/\sqrt{3}$, the boundary curve

$$\gamma_\alpha(\vartheta) = \left(\alpha\cos(\vartheta) - \tfrac{\alpha^3}{3}\cos(3\vartheta), -\alpha\sin(\vartheta) - \tfrac{\alpha^3}{3}\sin(3\vartheta), \alpha^2\cos(2\vartheta)\right), \quad \vartheta \in [0,2\pi) \tag{38}$$

has a convex projection to the $x$–$y$–plane, and for $1/\sqrt{3} < \alpha \le 1$ the projection is still injective. This yields uniqueness (of the minimal surface spanning $\gamma_\alpha$) for $0 < \alpha \le 1$, see [Ruc81]. For $\alpha > 1$ uniqueness of $X_E$ fails, i.e., at $\alpha = 1$ we have a (pitchfork, by symmetry) bifurcation of different minimal surfaces spanning $\gamma_\alpha$ [Nit76], see also [BT84].

In the demo `enneper` we choose $\alpha$ as a continuation/bifurcation parameter for

$$H(X) = 0, \quad \partial X = \gamma_\alpha, \tag{39}$$

see Fig.6. The problem (39) is "easy" in the sense that we have the explicit parametrization (37)

[5] see also Remark 3.7 for the Enneper–Weierstrass representation of Enneper's surface

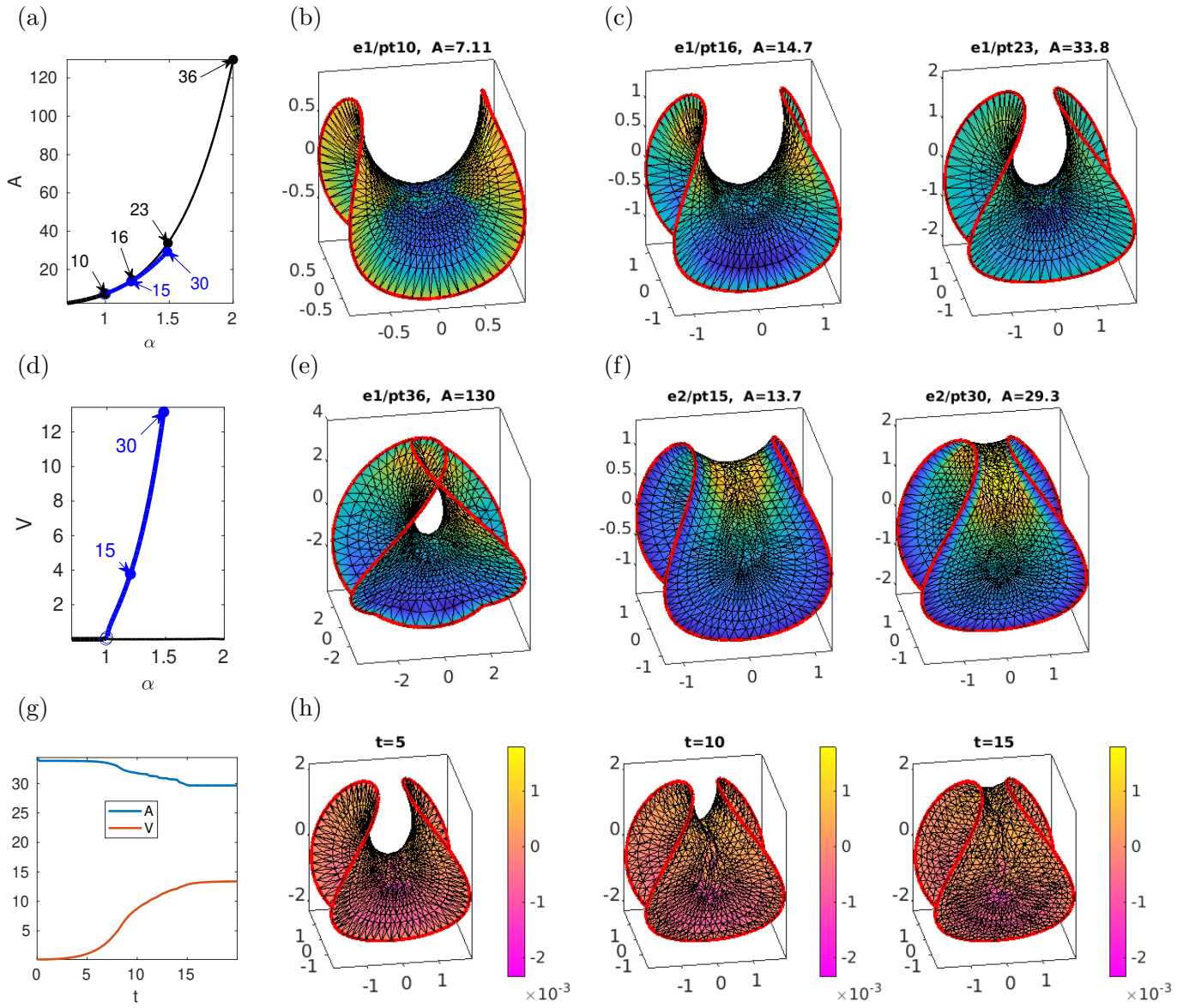


Figure 6: Bifurcation from the Enneper surface $X_E$, $A$ over $\alpha$ (a), and $V$ over $\alpha$ (d). At $\alpha = 1$ (`e1/pt10` in (b)), the branch `e1b` (blue) with smaller $A$ bifurcates from `e1` (black), samples in (b,c) and (e,f). (g,h) MCF from perturbation of `e1/pt23` to `e2/pt30`, samples showing $H$.

which we can use at any $\alpha$, but it requires care with the meshing, i.e., careful use of `refineX` and `degcoarsenX`, see §A.3. At $\alpha = 1$ we then find a supercritical pitchfork bifurcation from $X_E$, branch `e1` (black), to a branch `e2` (blue) which breaks the $(x, y, z) \mapsto (-y, x, -z)$ symmetry of $X_E$ (rotation by $\pi/2$ around the $z$ axis and mirroring at the $z = 0$ plane). The solutions "move up" (or down) in the middle, which decreases $A$ compared to $X_E$, cf. (c) vs (f). (d) illustrates that the (algebraic) volume $V$ of $X_E$ is always zero. The numerical continuation of `e1` to large $\alpha$ is no problem, using suitable mesh–adaption, even as $\gamma(\cdot;\alpha)$ self–intersects for $\alpha > \sqrt{3}$, because the associated parts of $X_E$ do not "see" each other, cf. (e) for an example. The continuation of `e2` to larger $\alpha$ is more difficult, and fails for $\alpha > 1.5$, as for instance shortly after `e1b/pt30` we can no longer automatically adapt the mesh near the top.

However, physically the change of stability at the symmetry breaking pitchfork at $\alpha = 1$ is most interesting. Using suitable combinations of `geomflow` (the MCF driver), `refineX`, `degcoarsenX` and `moveX`, see §A.3, we can use MCF to converge for $\alpha > 1$ and $t \to \infty$ to `e2`, from a variety of ICs, for instance from perturbations of `e1`, see Fig. 6(g,h), and `enneperflow.avi` in [MU24b], and after convergence we can then again continue the steady state.

## 3.3 Liquid bridges and nodoids

Weightless liquid bridges are CMC surfaces with prescribed boundary for instance consisting of two parallel circles wlog centered on the $z$-axis at a fixed distance $l$ and parallel to the $x$–$y$ plane. Additionally there is a volume constraint, which makes the problem different from Plateau's problem. See for instance [SAR97] and the references therein for physics background and results (experimental, numerical, and semi-analytical).

We consider liquid bridges between two fixed circles $C_1$ and $C_2$ of

$$\text{radius } r = r^* = 1, \text{ parallel to the } x\text{–}y \text{ axis and centered at } z = \pm l = \pm 1/2. \tag{40}$$

A trivial solution $X_0$ is the cylinder, with $H = 1/2$, volume $V = 2\pi l$ and area $A = 4\pi r l$ (without the top and bottom disks). Further explicit solutions are known in the class of surfaces of revolution, for instance nodoids. We first review some theory for nodoids with DBCs, and then continue basic liquid bridges (embedded nodoids), with bifurcations to non axial branches, see Figures 7 and 8. Nodoids with "periodic" BCs are studied in [MP02], and numerically in §3.3.3, where we also comment on the theory for these.

### 3.3.1 Nodoid theory

In [KPP17], a family of nodoids $\mathcal{N}(r, R)$ is parameterized by the neck (smallest) radius $r$ and the buckle (largest) radius $R$. Let $l > 0$ and $C_1, C_2 \subset \mathbb{R}^3$ be two circles of radius $r^*$ centered at heights $z = \pm l$ and parallel to the $x$–$y$ plane. With the two parameters $a, H \in \mathbb{R}$ the nodoids are parameterized by the nodary curve

$$(x, z) : [-t_0, t_0] \to \mathbb{R}^2, \quad \big(x(t), z(t)\big) = \left( \frac{\cos t + \sqrt{\cos^2 t + a}}{2|H|}, \frac{1}{2|H|} \int_0^t \frac{\cos\tau + \sqrt{\cos^2\tau + a}}{\sqrt{\cos^2\tau + a}} \cos\tau \, \mathrm{d}\tau \right), \tag{41}$$

which is then rotated around the $z$ axis, i.e.,

$$\mathcal{N}_{t_0} : M \to \mathbb{R}^3, \qquad (t, \theta) \mapsto \big(x(t)\cos\theta, x(t)\sin\theta, z(t)\big), \tag{42}$$

where $M = [-t_0, t_0] \times [0, 2\pi)$. Thus, in terms of §2.1 these nodoids are immersions of cylinders. While (41) only gives nodoids with an even number of self intersections (or none), shifting the $[-t_0, t_0]$ interval also gives odd numbers of self intersections. From the immersion $\mathcal{N}_{t_0}$, we can determine geometric quantities by evaluating the parametrization at the endpoints. For example, the height and the radius are given by

$$2l = \frac{1}{|H|} \int_0^{t_0} \frac{\cos t + \sqrt{\cos^2 t + a}}{\sqrt{\cos^2 t + a}} \cos t \, \mathrm{d}t, \quad r^* = \frac{\cos t_0 + \sqrt{\cos^2 t_0 + a}}{2|H|}, \tag{43}$$

and the buckle radius (at $t = 0$) is $R = \dfrac{1 + \sqrt{1 + a}}{2|H|}$. Implicitly, the equations in (43) define $a(t_0)$, hence also the mean curvature $H$, and thus $t_0$ parameterizes a family of nodoids $t_0 \mapsto \mathcal{N}_{t_0}$. Conversely, given $r, l$ in (40), the implicit equation

$$\frac{l}{2r}\left(\cos t_0 + \sqrt{\cos^2 t_0 + a}\right) - \left(\sin t_0 + \int_0^{t_0} \frac{\cos^2\tau}{\sqrt{\cos^2\tau + a}} \, \mathrm{d}\tau\right) = 0 \tag{44}$$

yields $a$ and $t_0$ which satisfy the boundary condition, and we exploit this to relate our numerics to results from [KPP17], see Remark 3.4.

In order to detect bifurcations from the family (42), we search for Jacobi fields vanishing on the boundary, cf. (19). The unit normal vector (field) of $\mathcal{N}_{t_0}$ is

$$N = \big(\cos t \cos\theta, \cos t \sin\theta, \sin t\big)\,, \quad t \in [-t_0, t_0),\ \vartheta \in [0, 2\pi),$$

and for every fixed vector $\vec{x} \in \mathbb{R}^3$, the function $\langle \vec{x}, N\rangle$ is a solution to (18). So the task is to find $\vec{x}$ and $t_0$ such that the Dirichlet BCs are fulfilled. The components of $N$ have zeros if the nodoid meets the boundary horizontally (parallel to the $x$–$y$ plane), which happens at $t_0 = \frac{\pi}{2} + k\pi$, or vertically, which happens at $t_0 = k\pi$ for $k \in \mathbb{N}$. Choosing the unit basis $(e_i)_{i=1,2,3}$, we have in the horizontal case that $\langle e_i, N\rangle\,|_{\partial\mathcal{N}_{t_0}} = 0$ for $i = 1, 2$, and in the vertical case $\langle e_3, N\rangle\,|_{\partial\mathcal{N}_{t_0}} = 0$.

**Lemma 3.2** *[KPP17, Lemma 3.4 and Proposition 3.6] Consider the one parameter family $\mathcal{N}_{t_0}$. If for some $t_0 \in \mathbb{R}_+$ the normal vector at $\partial\mathcal{N}_{t_0}$ is*

1. $N = \Big(0, 0, \nu(x)\Big)$, *then $L = \partial_u H(u)$ has a double zero eigenvalue.*
2. $N = \Big(\nu_1(x), \nu_2(x), 0\Big)$ *then $L = \partial_u H(u)$ has a simple zero eigenvalue.*

*The immersions are isolated degenerate, i.e., there exists an $\varepsilon > 0$ such that $(\mathcal{N}_t)_{t\in[t_0-\varepsilon,t_0+\varepsilon]}$ has a jump in the Morse index. In 1. this occurs for $t_0 = \frac{\pi}{2} + k\pi$, and in 2. for $t_0 = k\pi$, for every $k \in \mathbb{N}$.*

Now general bifurcation results (see the discussion after Lemma 2.2) yield the existence of bifurcation points at the horizontal and vertical cases presented in Lemma 3.2.

**Theorem 3.3** *[KPP17, Propositions 3.5 and 3.6] In cases 1. and 2. in Lemma 3.2 we have bifurcation points for the continuation in $H$. Moreover,*

1. *if $\psi = \langle e_i, N\rangle \in \ker L$ for $i = 1, 2$, then the bifurcating branch breaks the axial symmetry;*
2. *if $\psi = \langle e_3, N\rangle \in \ker L$, then the bifurcating branch breaks the $z \mapsto -z$ symmetry.*

### 3.3.2 Numerical continuation and bifurcation of nodoids

Nodoids with DBCs at the (fixed) top and bottom circles are treated in the demo `nodDBC`. For solutions without axial symmetry we additionally need to set a rotational phase condition (PC): If $X$ is a solution to (3), so is $R_\phi X$, where $\phi$ is the angle in the $x$–$y$ plane, and

$$R_\phi \vec{x} = \begin{pmatrix} \cos\phi & \sin\phi & 0 \\ -\sin\phi & \cos\phi & 0 \\ 0 & 0 & 1 \end{pmatrix} \vec{x}. \tag{45}$$

Thus, if $\partial_\phi(R_\phi X)|_{\phi=0} = \frac{1}{x^2+y^2}\,(-y\partial_x X + x\partial_y X) \in \mathbb{R}^3$ is non–zero, then it gives a non–trivial kernel of $L$, which makes continuation unreliable and bifurcation detection impossible. See, e.g., [Uec21b, §3.5] for further discussion of such continuous symmetries. Here, to remove the kernel we use the PC

$$q(u) := \int_X \langle \partial_\phi X_0, X_0 + uN_0\rangle \,\mathrm{d}S = \int_X \langle \partial_\phi X_0, N_0\rangle\, u \,\mathrm{d}S = \int_X \mathrm{d}\phi\ u \,\mathrm{d}S = 0, \tag{46}$$

where $X_0$ is from the last continuation step, with normal $N_0$, where $\phi$ is the angle in the $x$–$y$ plane, and hence $\partial_\phi X = -X_2\nabla_1 X + X_1\nabla_2 X$, where $\nabla_j$ are the components of the surface gradient, cf. (8). On the discrete level we thus obtain the linear function

$$q(u) = (\mathrm{d}\phi)^T u, \text{ with derivative } \partial_u q = (\mathrm{d}\phi)^T, \tag{47}$$

$\mathrm{d}\phi = \langle -X_2\nabla_{X_1}X + X_1\nabla_{X_2}X, N\rangle$, node–wise, i.e., $\nabla_{X_j}X$ is interpolated to the nodes. We then add $s_{\rm rot}q(u)$ to $E$ from (2) with Lagrange multiplier $s_{\rm rot}$, and thus modify the PDE to $G(u) := H(u) - H_0 + s_{\rm rot}\mathrm{d}\phi \stackrel{!}{=} 0$. This removes the $\phi$–rotations of non-axisymmetric $X$ from the kernel of $\partial_u G(u)$, and, moreover, $|s_{\rm rot}| < 10^{-8}$ for all the continuations below.

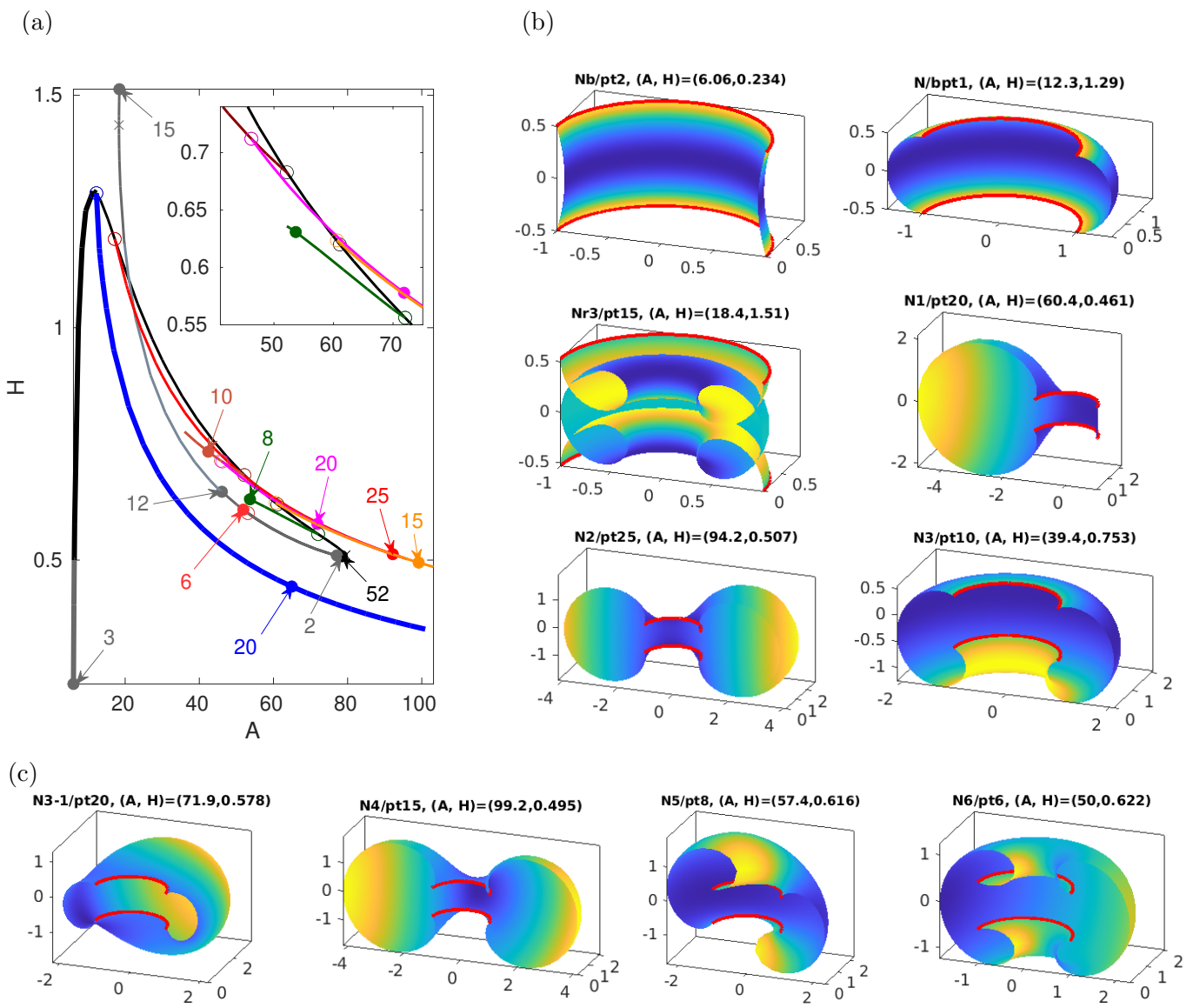


Figure 7: Bifurcation diagram of (mostly) embedded nodoids (a), with samples in (b,c) cut open at the $x$–$z$ plane ($y = 0$). Branches `N` (black), `Nb` (grey), `N1` (blue), `N2` (red), `N4` (orange), `N5` (green), `N6` (light blue), `N3-1` (magenta), and `Nr1`, `Nr2` and `Nr3` ("restarts" of `N`, grey). See text for details, and Fig. 8 for plots of `N/pt52`, `Nr1/pt2`, and `Nr2/pt12`.

Since the (algebraic) volume $V$ of self–intersecting nodoids is not intuitive, here we use continuation in area $A$ and $H$. Thus, we start with the constraint $q(u) = A(X) - A_0 \stackrel{!}{=} 0$, implemented in the `pde2path` library function `qfA`, with (action of the) derivative $q'(u)v = -2\int_X H_0 v\,\mathrm{d}S$, implemented in `qjacA`. For non–axisymmetric branches we set up `qfArot` and its derivative, where we put (46) as a second component of `qfA`, and similarly for the derivatives, and when we bifurcate to a non-axisymmetric branch, we set `p.nc.nq=2` (2 constraints, area and rotational phase) and `p.fuha.qf=@qfArot`.

Figure 7 shows results from `cmds1.m` (see also the movie `nodDBCs.avi` from [MU24b] to go step by step through the bifurcation diagram). We start at the cylinder and first continue to larger $A$ (black branch `N`). The first BP at $(A, H) \approx (12.24, 1.29)$ is double with angular wave number $m = 1$. We

simply select one of the kernel vectors to bifurcate, see §A.1, and do two steps without PC, and then switch on the rotational PC and continue further (blue branch `N1`). As predicted, BP1 occurs when $X$ meets the lower and upper boundary circles horizontally, and the stability changes from `N` to `N1`.[6] The second BP yields the $m = 2$ branch `N2` (red). These results fully agree with those from [Bru18]. The branch `Nb` (grey, with `pt3`) is the continuation of `N` to smaller $A$ (and $V$), where the cylinder curves inward.

The third BP on `N` is simple with $z \mapsto -z$ symmetry breaking, yielding branch `N3` (brown). On `N3` there are secondary bifurcations, and following the first we obtain `N3-1` (magenta). The 4th BP on `N` again has $m = 2$ but is different from the 2nd BP on `N` as the nodoid has already "curved in" at the boundary circles, which is inherited by the bifurcating branch `N4` (orange). The 5th BP on `N` yields a skewed $m = 2$ nodoid `N5` (green).[7] After the fold, the mesh in `N` becomes bad at the necks, see `N/pt52` in Fig. 8. Thus, for accurate continuation we use (42) to remesh, see `Nr1/pt2` and Remark 3.4(a) and Fig. 8(a–c), yielding the branch `Nr1` (grey) in Fig. 7(a). `Nr1/pt12` in Fig. 8 shows that after a number of steps the mesh at the neck deteriorates again, and so we remesh again to `Nr2` (light grey). The nodoid then self–intersects at $(A, H) \approx (22.9, 1.05)$, and at `Nr2/pt10` we do the next restart to `Nr3`. Using such remeshing we can continue the branch `N` (as `Nr1, Nr2, Nr3, ...`) to many loops and self–intersections, with many further BPs as predicted in Lemma 3.2. In Fig. 8(d) we illustrate the correspondence of our numerical results for the continuation in $A$ to Theorem 3.3, see Remark 3.4(b).

**Remark 3.4** a) For axi– and $Z_2$ symmetric nodoids, we can extract $a{=}(2HR{-}1)^2 - 1$ from our numerical data, with $R$ the radius on the $z{=}0$ plane. We can then numerically solve the second equation in (43), i.e., $1 = r^* = \dfrac{\cos t_0 + \sqrt{\cos^2 t_0 + a}}{2|H|}$ for $t_0$, and use this for restarts with a new mesh, for instance from `N/pt52` to `Nr1/pt1` in Fig. 8.

b) Similarly, given $r^*{=}1$ and $l{=}0.5$, we can solve (44) for $a$ and $t_0$ in a continuation process. Then computing $A{=}A(a, t_0)$ gives the black curve in Fig. 8(d), and intersecting the $A$ values of our numerical BPs gives the $t_0$ values for BP1, BP3 and BP6 as predicted, and explains the folds FP1 and FP2. In summary, the BPs on `N`, their multiplicities, and their relation to Theorem 3.3 (if applicable) are

| BP number | BP1 | BP2 | BP3 | BP4 | BP5 | BP6 |
|---|---|---|---|---|---|---|
| multiplicity | 2 | 2 | 1 | 2 | 2 | 2 |
| Theorem 3.3 | 1. | NA | 2. | NA | NA | 1. |
| $t_0$ | $\pi/2$ | 1.995 | $\pi$ | 3.377 | 3.622 | $3\pi/2$ |

(48)

where NA means not applicable, and where for BP1, BP3 and BP6 we give the exact values, with as indicated in Fig. 8(d) very good agreement of the numerics.[8] ⌋

### 3.3.3 Nodoids with periodic BCs in $z$

In [MP02], bifurcations of axisymmetric to non–axisymmetric nodoids are studied with the period (the "height") along the axis of revolution (wlog the $z$–axis) as the continuation/bifurcation parameter. For fixed $H = 1$, [MP02] proves that there is a $r_0 > 0$ such that for neck radii $r > r_0$ ($r < r_0$) there are (are not) bifurcations from nodoids, and gives detailed asymptotics of bifurcation points in a regime ($\tau \to -\infty$ in [MP02]) which corresponds to $(R - r)/R \to 0$ with outer radius $R$, see below. In particular, the 2nd variation of the area functional around a given nodoid $\mathcal{N}_\tau$ is analyzed with

[6] `N` up to `BP1`, `Nb`, and `N1` are the only stable (in the sense of volume preserving MCF) branches in Fig. 7, and hence physically most relevant; the further branches we compute are all unstable, and hence of rather mathematical than physical interest.

[7] BP5 is an example of a BP qualitatively predicted in [KPP17, Prop.3.9] at large $t_0$.

[8] This also holds for further BPs and folds, but we refrain from plotting these in the already cluttered BD in Fig. 7.

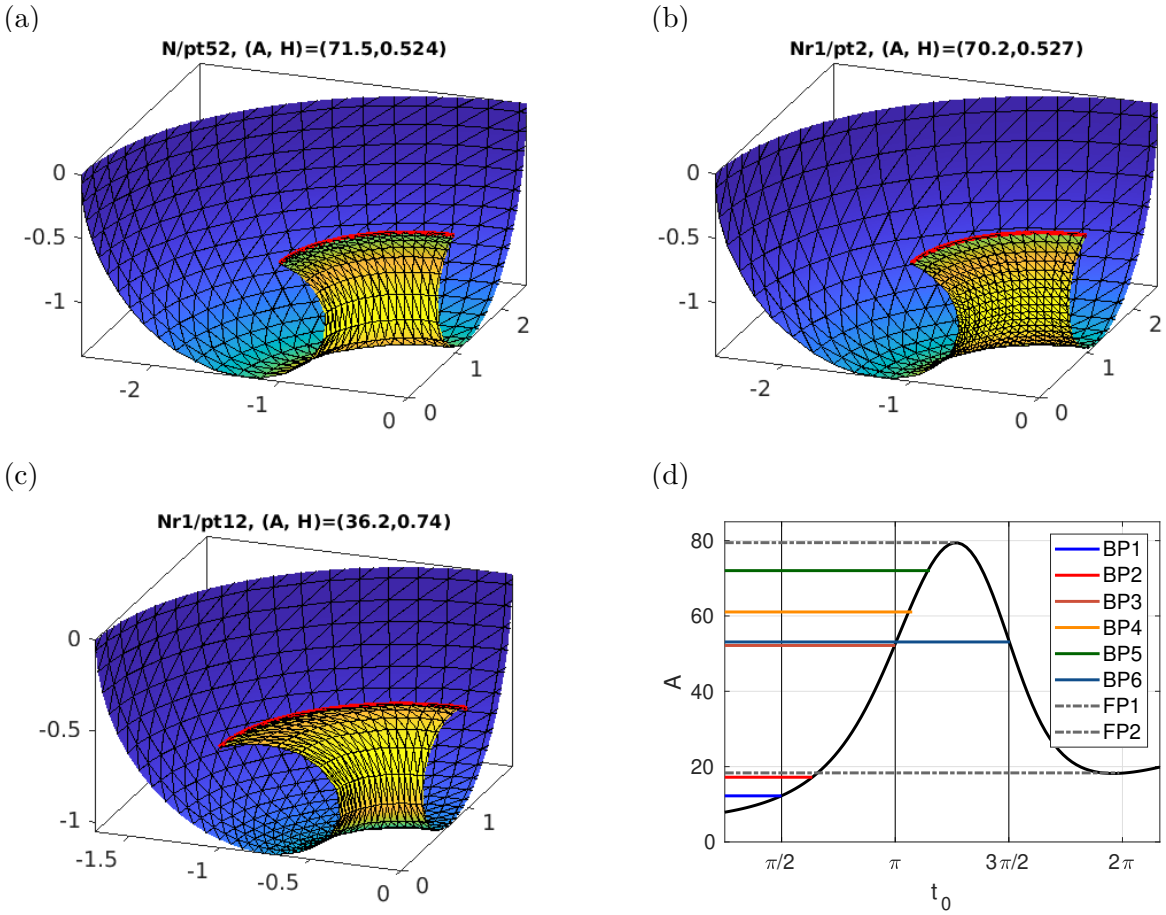


Figure 8: Continuation of Fig.7; (a–c) (1/8th of) solutions on `N` before and after remeshing. (d) Comparison to analytical results, see Rem. 3.4(b).

$z \in \mathbb{R}$, i.e., for the full non–compact nodoid, not just for one period cell. This proceeds by Bloch wave analysis, and first establishes the band structure of the spectrum. Using a parametrization similar to (41), a detailed analysis of the second variation of the area functional, and ultimately two different numerical methods, [Ros05] shows that $r_0 = 1/2$, and the first bifurcation (at $r_0$) leads to non–axisymmetric nodoids with angular wave number $m = 2$ and same periodicity in $z$, i.e., Bloch wave number $\alpha = 0$ in [MP02].

Here we also consider periodic (in $z$) nodoids with fixed $H = 1$ using the height $\delta$ as continuation/bifurcation parameter. We recover the primary bifurcation at $r = r_0 = 1/2$ from [Ros05], and find further bifurcations. Numerically, to set up "periodic boundary conditions in $z$", we proceed similar to the `pde2path` setup for periodic boundary conditions on fixed domains, see [Uec21b, §4.3]. The basic idea is to identify points on $\partial X$ at $z = \pm\delta$. Thus, before the main step $X_0 \mapsto X_0 + uN_0$ for all our computations, we transfer the values of $u$ from $\{X_3 = -\delta/2\}$ to $\{X_3 = \delta/2\}$ via a suitable "fill" matrix `p.mat.fill`, which has to be generated at initialization and regenerated after mesh–adaptation. Similar to §3.3.2 we need a rotational PC for non–axisymmetric branches, but here for all computations we additionally need translational PCs in $x, y$ and $z$ directions, i.e. $T_i\vec{x} = \vec{x} + \delta e_i$. These translations act infinitesimally in the tangent bundle as $T_i X_0 = \nabla_i X_0$, and hence the pertinent PCs are

$$q_i(u) := \langle \nabla_i X_0, X_0 + uN_0 \rangle = \langle \nabla_i X_0, N_0 \rangle\, u = 0, \quad i = 1, 2, 3, \tag{49}$$

with derivatives $\partial_u q_i(u) = \langle \nabla_i X_0, N_0 \rangle$. Like (47), they are implemented node–wise, and their derivatives are added to $G$ with Lagrange multipliers $s_x, s_y, s_z$.

Figure 9 shows some results from `nodpBC/cmds1.m`. For robustness (essentially due to the strong

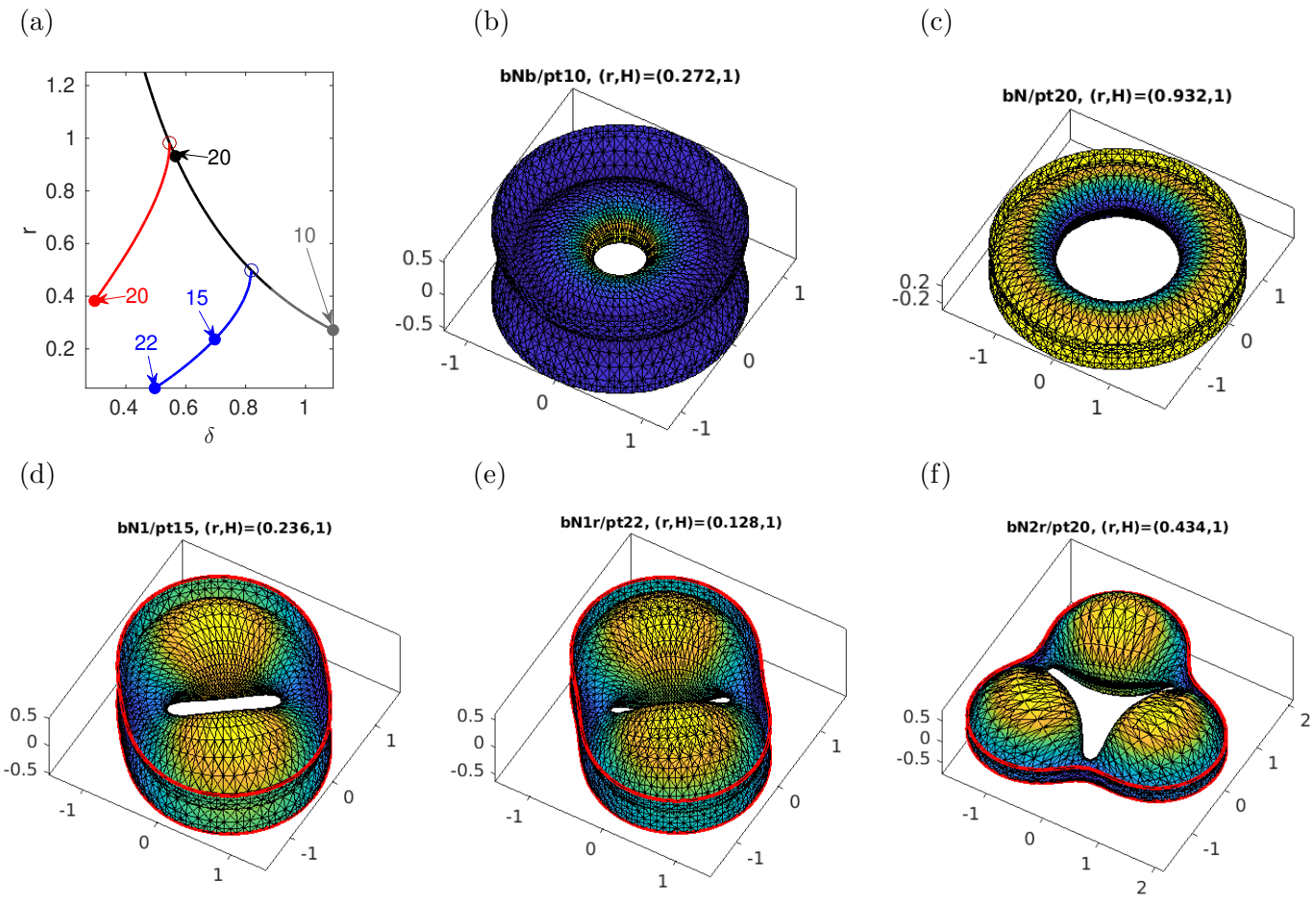


Figure 9: (a) Bifurcation diagram of nodoids parametrized by height $\delta$, fixed $H = 1$. The axisymmetric branch `bN` (black) starts near $\delta = 0.88$ via (42), and in direction of decreasing $\delta$ shows a sequence of BPs to nodoids with broken $S^1$ symmetry, here `bN1` (blue, $m = 2$) and `bN2` (red, $m = 3$). Samples in (b–f), with `bN1r` and `bN2r` after some refinement.

contractions at the inner loops later in the branches) it turns out to be useful to initialize with a rather coarse mesh and after 1 or 2 steps refine by area. As we then decrease $\delta$ from the initial $\delta \approx 0.88$, we find the first BP at $\delta \approx 0.82$ and with $r = 0.5$, corroborating [Ros05], to the angular wave number $m = 2$ branch `bN1`. Using mesh refinement along the way we can continue `bN1` to small $\delta$, where in particular we have multiple self–intersections; first, the inner loops extend the "height" $\delta$ for $\delta < \delta_0 \approx 0.78$, and second the inner loops intersect in the plane $z = 0$ for $\delta < \delta_1 \approx 0.43$ (not shown), making the inner radius $r = 0$ (or rather undefined). The branch `bN2` from the next BP at $\delta \approx 0.54$ has $m = 3$, and otherwise behaves like the $m = 2$ branch. All these branches are rather strongly unstable, with $\mathrm{ind}(X) > 4$, and Footnote 6 again applies.

**Remark 3.5** The branching behavior of the periodic nodoids very much depends on which period cell in $z$ we prescribe, with Fig. 9 corresponding to one cell. Naturally, all 1–periodic solutions are $n$–periodic for any $n \in \mathbb{N}$. With respect to bifurcations, the 1–cell computations then correspond to Bloch wave numbers $\alpha = 0$ in [MP02]. For $n \geq 2$ periods cells we obtain further discrete Bloch wave numbers, e.g., additionally $\alpha = \pi$ for $n = 2$. This then allows bifurcations which simultaneously break the $S^1$ and the $Z_2$ symmetry of the symmetric nodoid, and this is illustrated in [MU24a, Fig.14], giving a basic impression of the extremely rich bifurcation picture to be expected when the computational cell is expanded further in $z$. ⌋

## 3.4 Triply periodic surfaces

Triply periodic surfaces (TPS) are CMC surfaces in $\mathbb{R}^3$ which are periodic wrt three independent directions. Triply periodic *minimal* surfaces (TPMS) (this implicitly also means embedded, sometimes abbreviated as TPEMS) have been studied since H.A. Schwarz in the 19th century, and have found renewed interest partly due to the discovery of new TPMS by A. Schoen in the 1970ies, and due to important (partly speculative) applications of TPMS (and their non–zero $H$ TPS companions) in crystallography, mechanics and biology. See for instance [AHLL88] and [STFH06], and [Bra23] for a long list of TPMS.

From the PDE point of view, TPS solve (3) with periodic BCs on a bounding box. Some families of TPMS were studied analytically as bifurcation problems in [KPS18], using a cell length (period) in one direction as continuation/bifurcation parameter, and combined with numerical results from [ES18]. Much of the theory of TPMS is based on Enneper–Weierstrass representations. See Remark 3.7, where we relate some of our numerical results for the Schwarz P surface family to results from [KPS18] obtained via Enneper–Weierstrass representations.

A way to *approximate* TPS is as zeros of Fourier expansions of the form

$$F(\vec{x}) = \sum_{k\in\mathbb{Z}^3, |k|\leq N} F(k)\cos(2\pi k\cdot\vec{x} - \alpha(\vec{x})).$$

A simple first order approximation of the Schwarz P surface (cf. Fig.1(d)) is

$$\text{Schwarz P} \approx \{(x,y,z)\in\mathbb{R}^3 : \cos(x)+\cos(y)+\cos(z)=0\}, \tag{50}$$

Better approximations with some higher order terms are known, also for many other "standard" TPS, see, e.g., [GBMK01] for a quantitative evaluation of such approximations.[9]

### 3.4.1 The Schwarz P minimal surface (family)

In `TPS/cmds1.m` we study continuation (and bifurcation) of the Schwarz P surface in the period $\delta$ in $z$–direction, focusing on one period cell, i.e., the box

$$B_\delta := [-\pi,\pi)^2 \times [-\delta/2, \delta/2). \tag{51}$$

To get an initial (approximate) $X$ on $B_{2\pi}$, we use (50) and the mesh generator `distmesh` [PS04], on one eighth of $B_{2\pi}$, which we then mirror to $B_{2\pi}$. The continuation in $\delta$ proceeds similar to §3.3.3, by first scaling $X = S_\delta$`p.X` to period $\delta$ in $z$ and then setting $X = X + uN$ and solving for $(u,\delta)$. As in §3.3.3 we have translational invariance in $x, y$ and $z$, and hence exactly the same PCs.

Somewhat differently from §3.3.3 we now also "fill" $X$ by taking the $\partial X$ values from the left/bottom/front of the box to the right/top/back of the box. While $u$ is still filled via $u =$ `p.mat.fill`$*u$, for filling $X$ we compute matrices `p.Xfillx, p.Xfilly, p.Xfillz` similar to `p.mat.fill`, but with $-1$ (instead of 1) where we want to transfer $X$ values from one side of the box to the opposite side (assuming symmetry wrt the origin). Finally, it turns out that the continuation is more robust if we correct $N$ at the boundaries to lie *in* the boundaries of $B_\delta$, see Remark 3.6.

Figure 10 shows some results from `TPS/cmds1.m`. Decreasing $\delta$ from $2\pi$ (`P/pt1` in (b) at $\delta = 6.2732$), $X$ gets squashed in $z$ direction, and at $\delta = \delta_1 \approx 5.9146$ we find a $D_4$ symmetry breaking pitchfork bifurcation (with the two directions corresponding to interchanging the $x$ and $y$ axis wrt

[9] The approximation (50), and higher order corrections, also arise from solving the amplitude equations for a Turing bifurcation on a simple cubic (SC) lattice, where hence the Schwarz P surface, or, depending on volume fractions a CMC companion of Schwarz P, occurs as the phase separator between "hot" and "cold" phases. See, e.g., [CK97] and [Uec21b, §8.1,8.2], and similarly [WBD97] for the occurrence of Scherk's surface in 3D Turing patterns.

shrinking and expansion) to a branch `P1`, which then extends to large $\delta$. On the other hand, increasing $\delta$ from $2\pi$ (branch `pB`, grey), we find a fold on the P branch at $\delta = \delta_f \approx 6.408$. Both $\delta$ values agree well with results from [KPS18] based on the Enneper–Weierstrass representation, summarized in Fig. 10(h), see Remark 3.7.

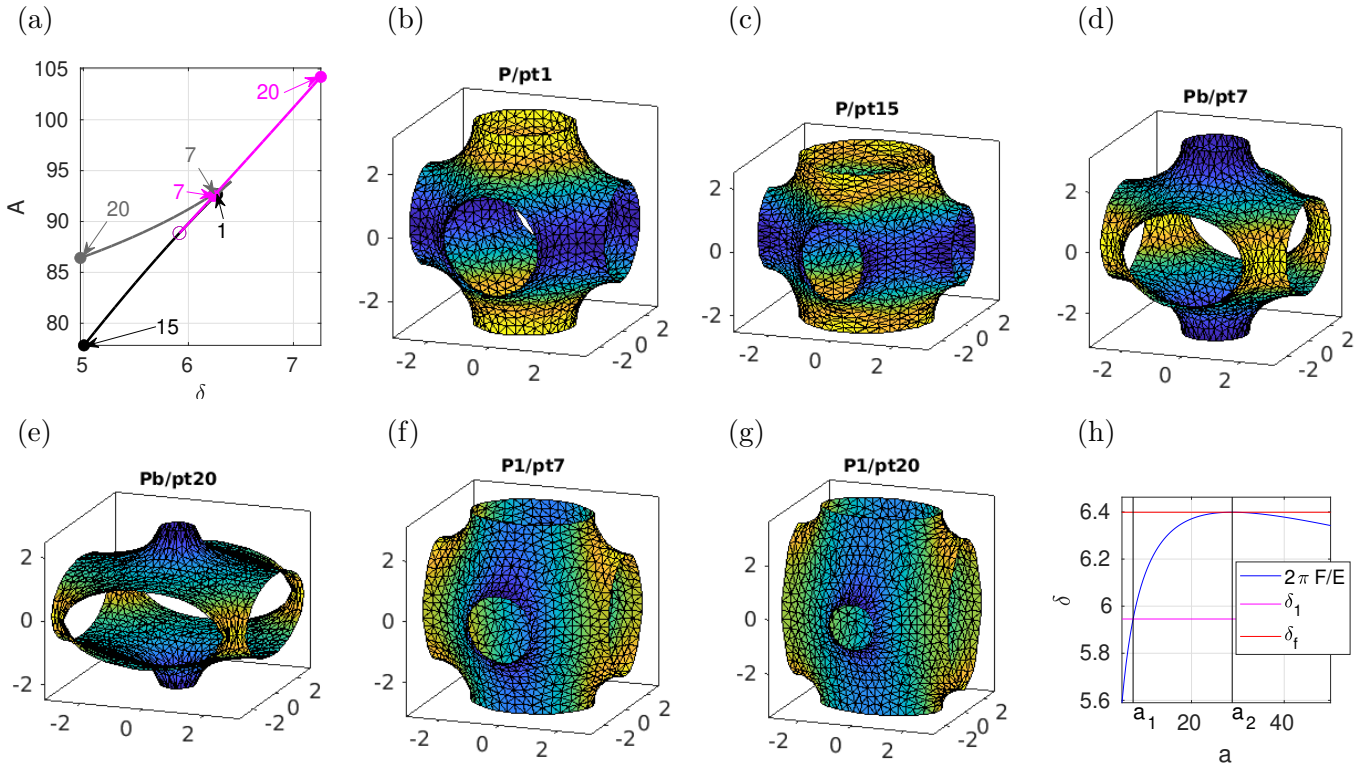


Figure 10: (a) Bifurcations in the Schwarz P family, black (P) and grey (Pb) branch; bifurcating magenta branch (P1) breaks $D_4$ symmetry. Samples in (b–g). Comparison with [KPS18] in (h), cf. Remark 3.7.

**Remark 3.6** a) The results from Fig. 10 can also be obtained by choosing "Neumann" BCs on $\partial B_\delta$. However, for other TPMS we need the pBCs. For instance, we can also continue the H surface family on a suitable (almost minimal) rectangular box, where solutions fulfill pBCs but not Neumann BCs. Due to the necessary larger period cell, and due to branch points of higher multiplicity, the numerics for the H family are more elaborate, and these results will be presented elsewhere.

b) In the local copy `TPS/getN.m` we apply a trick and zero out $N_1$ at $x = \pm\pi$, $N_2$ at $y = \pm\pi$ and $N_3$ at $z = \pm\delta/2$. Thus, $N$ is forced to always lie in the cube's faces, yielding a "combination of NBCs and pBCs" in the sense that the trick forces $X$ to meet the cube's faces orthogonally, while the pBCs keep $X$ on opposite faces together. However, the trick is for convenience as without it we get the same branches but in a less robust way, i.e., requiring finer discretizations and smaller continuation stepsizes. ⌋

**Remark 3.7** The Enneper–Weierstrass representation of a minimal surface is

$$\big(x, y, z\big) = \mathrm{Re}\Big[\mathrm{e}^{\mathrm{i}\vartheta} \int_{p_0}^{p} (1 - z^2,\, \mathrm{i}(1 + z^2),\, 2z) R(z)\, \mathrm{d}z\Big], \tag{52}$$

$p_0, p \in \mathcal{M}$ with $\mathcal{M}$ a Riemannian surface, where $\vartheta$ is called Bonnet angle, and $R : \mathcal{M} \to \mathbb{C}$ is called Weierstrass function. The Enneper surface $E$ from §3.2 is given by the data $\mathcal{M} = D_\alpha$ (disk of radius $\alpha$) and $R(z) \equiv 1$. For TPMS, $R$ is a meromorphic function, and $\mathcal{M}$ consists of sheets connected at branch points given by poles of $R$. See, e.g., [Oss14, §8] for a very readable introduction to Weierstrass

data and the connection of minimal surfaces and holomorphic functions, [Hof90] for a basic discussion of the Weierstrass data of TPMS, [Ros92] for identifying the Riemannian surface $\mathcal{M}$ for the Schwarz P surface with $S^2 \times S^2$ by stereographic projection, where $S^2$ is the unit sphere, and [FW14] for further examples for construction of TPMS from Weierstrass data.

Following [KPS18], we consider $\mathcal{M}$ a double cover of $\mathbb{C}$, and, for $a \in (2, \infty)$, let

$$R(z) = 1/\sqrt{z^8 + az^4 + 1}, \tag{53}$$

where the Schwarz P surface with period cell $[-\pi, \pi)^3$ is obtained for $\vartheta = 0$ and $a = 14$.[10] See also [GK00] for the explicit computation of a fundamental patch of Schwarz P based on (52) and (53) with $a = 14$ and a small planar preimage $\subset \mathbb{C}$.

In [KPS18], $a$ is taken as a bifurcation parameter along the Schwarz P family with the periods for Schwarz P given by [KPS18, §7.3]

$$E = 2\int_0^1 \frac{1-t^2}{\sqrt{t^8+at^4+1}}\,\mathrm{d}t + 4\int_0^1 \frac{\mathrm{d}t}{\sqrt{16t^4-16t^2+2+a}} \quad \text{(periods in } x \text{ and } y\text{)}, \tag{54}$$

$$F = 8\int_0^1 \frac{t}{\sqrt{t^8+at^4+1}}\,\mathrm{d}t \quad \text{(period in } z\text{)}, \tag{55}$$

up to homotheties (uniform scaling in all directions). We have $\delta = 2\pi F/E$ for our $\delta$, and evaluating $E, F$ numerically (or as elliptic integrals) and plotting $\delta(a) := 2\pi F/E$ as a function of $a$ we get the blue curve in Fig. 10(h), which corresponds to [KPS18, Fig.13]. In particular, $\delta(a)$ has a maximum at $a = a_2 \approx 28.778$, and $\delta(a_2) = \delta_f$ completely agrees with our fold position in Fig. 10(a). On the other hand, with suitable mesh adaptation the branch P1 continues to at least $\delta = 10$. Next, [KPS18] based on [ES18] gives a bifurcation from the P family at $a = a_1 \approx 7.4028$, and again we find excellent agreement $\delta(a_1) = \delta_1$ with our BP at $\delta_1$. ⌋

**Remark 3.8** a) The fact that the Schwarz P family does not extend to "large" $\delta$ (but folds back) has also been explained geometrically in [Hof90], without computation of the fold position.

b) The stability of Schwarz P (and hence also Schwarz D) on a minimal period cell and wrt *volume preserving* variations is shown in [Ros92]. However, "larger pieces" of P, e.g., P on $[-\pi, \pi)^2 \times [-2\pi, 2\pi)$ are *always* unstable, even wrt volume preserving variations. See also [Bra96, §8] for a useful discussion, and illustrations. Numerically, in Fig. 10 we find: $\mathrm{ind}(X) = 2$ except on the segment $\mathcal{S}$ of P (and Pb) between the fold and the BP at $\delta_1$, where $\mathrm{ind}(X) = 1$. However, the most (and on $\mathcal{S}$ only) unstable eigenvector has a sign (see [MU24a] for plots), and hence the solutions on $\mathcal{S}$ are stable wrt volume preserving variations. ⌋

### 3.4.2 CMC companions of Schwarz P

In Fig.11 we show some CMC companions of Schwarz P. Continuing first to smaller $H$ (black branch `PH`), $X$ (the volume enclosed by $X$ and the boundaries of the cube) "shrinks" and we find a BP at $H \approx -0.1$. In the other direction (grey branch `PHb`), $X$ (the volume enclosed by $X$) "expands", with a BP at $H \approx 0.1$. The continuation of both these branches fails at $H \approx -0.3$ and $H \approx 0.3$ (respectively), though they can be continued slightly further with careful mesh adaptation.

Our main purpose here is to show how symmetry considerations and some tricks can help to avoid numerical pitfalls. By symmetry, the BP `PH/bpt1` (and similarly `PHb/bpt1`) must be double, although

[10] For $\vartheta = \pi/2$ we obtain the Schwarz D family, and for $\vartheta \approx 0.9073$ Schoen's gyroid, as two further TPMS. Moreover, since these have the same Jacobians as Schwarz P, all bifurcation results from Schwarz P carry over to Schwarz D and the gyroid, but these appear to be much more difficult to treat in our numerical setting.

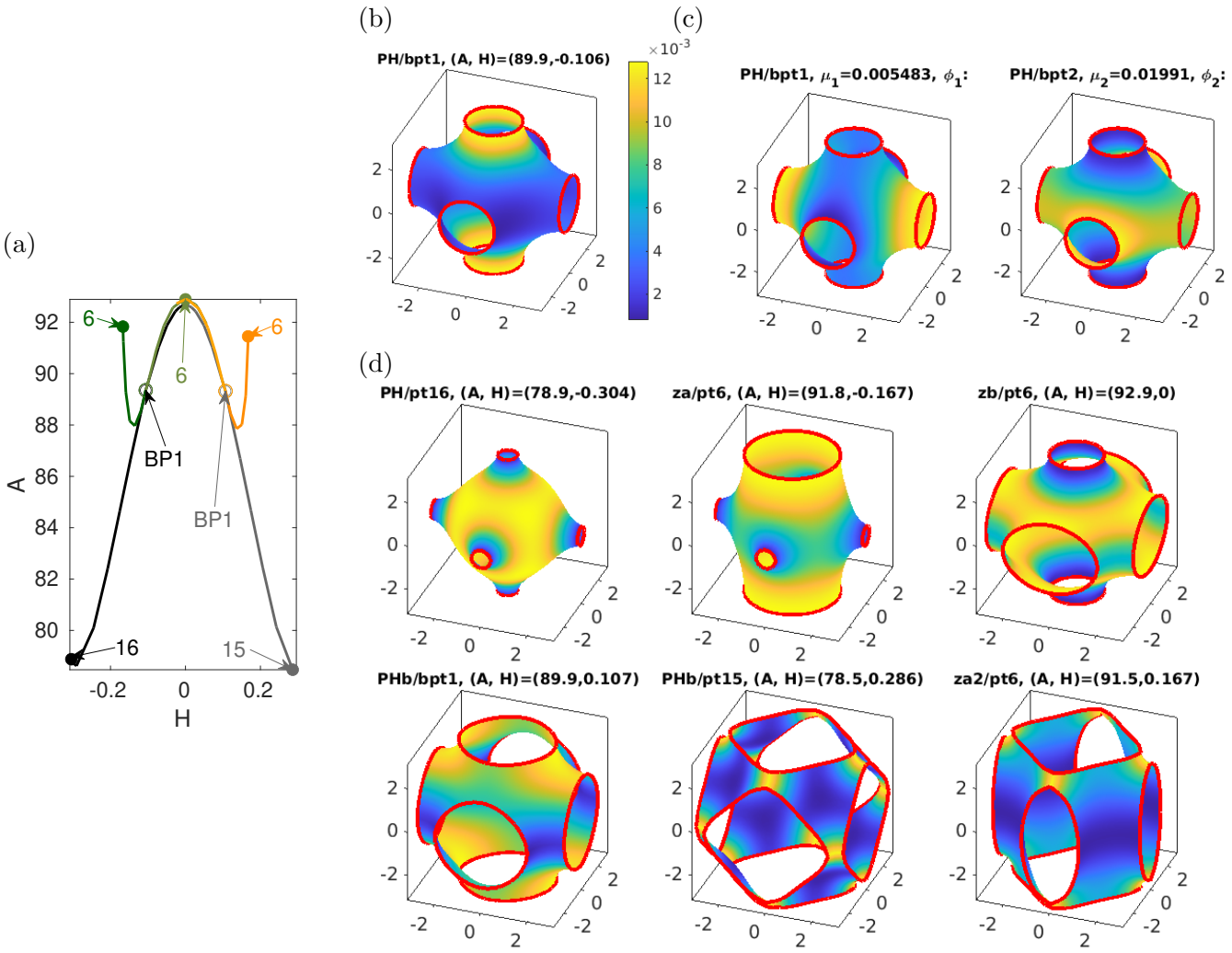


Figure 11: Results from `TPS/cmds2.m`. Continuation of Schwarz P in $H$ at fixed $\delta{=}2\pi$. BD in (a): `PH` (black), `PHb` (grey), `za` (dark green) and `zb` (lighter green), and `za2` and `zb2` (orange), which altogether are only two different branches. BP1 on `PH` and approximate kernel vectors in (b,c), and further samples in (d).

the smallest (in modulus) eigenvalues reported at `PH/bpt1` are $\mu_1 \approx 0.005$ and $\mu_2 = 0.02$.[11] See Fig.11(b) for `PH/bpt1`, and (c) for the (approximate) kernel vectors $\phi_1$, $\phi_2$. In fact, the plot in (b) (stronger correction along the $z$–axis) shows that at least the last step in the localization of `PH/bpt1` violated the $S_4$ symmetry of the (now fixed) cube, which explains the rather significant splitting of the in principle double eigenvalue $\mu_1 = 0$. Clearly, we expect $\phi_{1,2}$ to approximate two bifurcation directions, with $D_4$ symmetry along the $x$ axis ($\phi_1$) and $y$ axis ($\phi_2$). By symmetry we then must have at least one more bifurcating branch, with $D_4$ symmetry along the $z$ axis. To find this bifurcation direction, we can use `qswibra` with numerical derivation and solution of the algebraic bifurcation equation (ABE) [Uec21b, §3.2.2]. However, this is expensive and not always reliable. Here, the three bifurcation directions (oriented along $x$, along $y$, and along $z$) *are* returned, but we have to relax the tolerance `isotol` for identifying solutions of the ABE as isolated. Alternatively, we can just compute and plot the (approximate) kernel vectors $\phi_1, \phi_2$, which lets us guess to approximate the third direction as $\phi_3 = 0.2\phi_1 + \phi_2$. This turns out to be sufficiently accurate and gives the transcritical branch(es) `za` (dark green) and `zb` (other direction, lighter green).

On `za`, the continuation fails after `pt6`. `zb/pt6` is at $H = 0$ and corresponds to `Pb/pt7` from Fig. 10. Subsequently, `zb` continues to `PHb/bpt1`, and is indeed identical to the branch(es) `za2` (and

[11] Additionally, there is a simple negative eigenvalue $\mu_0 \approx -0.7$, and the next two eigenvalues are $\mu_{3,4} \approx 0.5$, i.e., $\mu_{1,2}$ are well separated from the rest of the spectrum.

zb2), transcritically bifurcating there. In particular, PHb/bpt1 is again double, and we can compute the three branches oriented along $x, y$ or $z$ as above (see cmds2.m). zb2 (light orange) then continues back to PH/bpt1, while zb2 fails after pt6 (last sample in (d)). The continuation failures of za and za2 after pt6 are due to poor meshes as the different boundaries of $X$ come close to each other, like after PH/pt16 and PHb/pt15, and it seems difficult to automatically adapt these meshes.

# 4 Fourth order biomembranes

The (dimensionless) Helfrich (or spontaneous curvature (SC)) functional [Hel73] is

$$E := \int_X (H - c_0)^2 + bK \,\mathrm{d}S, \tag{56}$$

where $c_0 \in \mathbb{R}$ is called spontaneous curvature, and $b \in \mathbb{R}$ is called saddle–splay modulus. The motivation of (56) are the shapes of closed vesicles with a lipid bilayer membrane, for instance red blood cells (RBCs), for which $E$ is to be minimized under the constraints of fixed area $A(X) - A_0 = 0$ and enclosed volume $V(X) - V_0 = 0$. This motivated much work, e.g., [SBL90, Sei97, NT03, VDM08, OYT14], aiming to understand the various shapes of RBCs[12], mostly in the axisymmetric case. Applying our algorithms to closed vesicles (without a priori enforcing any symmetry) we recover many of the results from the above references. See also [LWM08, KIPM$^+$20] for further biological and mechanical background, [JQJZC98] for non–axisymmetric shapes (under different constraints), and [FVKG22] for the related problem of 1D radial wrinkling of arteries, with an additional restoring force due to the surrounding tissue, and a very rich bifurcation structure.

For closed $X$, the term $b\int_X K \,\mathrm{d}S$ in (56) can be dropped due to the Gauss–Bonnet theorem, cf. Footnote 1, as $\int_X K \,\mathrm{d}S = 2\pi\chi(X)$ is a topological constant, such that the Lagrangian is

$$F = \int_X (H - c_0)^2 \,\mathrm{d}S + \lambda_1(A - A_0) + \lambda_2(V - V_0), \tag{57}$$

where $\lambda_1$ (corresponding to a surface tension) and $\lambda_2$ (corresponding to a pressure difference between outside and inside) are Lagrange multipliers for area and volume constraints. The Euler-Lagrange equation is

$$\Delta H + 2H(H^2 - K) + 2c_0K - 2c_0^2H - 2\lambda_1 H - \lambda_2 = 0. \tag{58}$$

If $X$ is not closed, then often one or both of the constraints $A - A_0 = 0$ and $V - V_0 = 0$ is (are) dropped, and the associated Lagrange multipliers $\lambda_{1,2}$ are treated as external parameters, often with $\lambda_2 = 0$. If in the Gauss–Bonnet formula

$$\int_X K \,\mathrm{d}S = 2\pi\chi(X) - \int_{\partial X} \kappa_g \,\mathrm{d}s \tag{59}$$

we assume $\gamma = \partial X$ to be parameterized by arclength, then the geodesic curvature $\kappa_g$ is the projection of the curvature vector $\gamma''(\vec{x})$ onto the tangent plane $T_{\vec{x}}(X)$, see, e.g., [Tap16, §4.3]. If as before we restrict to normal variations $\psi = uN$, which moreover fix the boundary, i.e.,

$$u|_{\partial X} = 0, \tag{60}$$

[12] or, more down to earth, lipid bilayer membrane vesicles which develop upon injection of lipids into water, and which for instance can also organize into tubes; see also [SL95, §8] for a discussion of additional structures (networks of spectrin tetramers) on the membrane of RBCs

then

$$\partial_\psi F = \int_X (\Delta H + 2H(H^2 - K) + 2c_0 K - 2Hc_0^2 - 2\lambda_1 H)u \,\mathrm{d}S + \int_{\partial X} (H - c_0 + b\kappa_n)\partial_n u \,\mathrm{d}s,$$

where $\kappa_n = \langle \gamma'', N\rangle$ is the normal curvature of $\gamma = \partial X$, i.e., the projection of the curvature vector onto the normal plane, see, e.g., [PP22] and the references therein. Thus we again obtain (58) (with $\lambda_2 = 0$), and additionally to (60) we can consider either of

$$\partial_n u = 0 \text{ on } \partial X \text{ (clamped BCs, i.e., Neumann BCs)}, \tag{61}$$

$$H - c_0 + b\kappa_n = 0 \text{ on } \partial X \text{ (stress free BCs)}. \tag{62}$$

In case (61) we have $\int_{\partial X} \kappa_g \,\mathrm{d}s = 0$ in (59), and hence $\int bK \,\mathrm{d}S$ again becomes constant and can be dropped from (56).

In §4.1 we focus on closed vesicles, and in §4.2 on "Helfrich caps", i.e., disk type solutions of (58) with BCs (60) and (62). In [MU24a, §3.6] we also consider "Helfrich cylinders", i.e., a cylindrical topology with BCs (60) and (61).

**Remark 4.1** a) With $N$ the inner normal, the stability for (58) refers to the Helfrich flow (see, e.g., [KN06] for the existence theory near spheres) $\left\langle \dot{X}, N \right\rangle = -(\Delta H + 2H(H^2 - K) + 2c_0 K - 2c_0^2 H - 2\lambda_1 H)$, with BCs (60), and (61) or (62), for non–closed vesicles.

b) Biological vesicles can undergo topological transitions which are important for their biological function, e.g., fission of a small bud from the vesicle, or fusion of two vesicles. We cannot capture such transitions in our setup of steady state continuation. Some examples of splitting in DNS for a phase field model are given in [DLW06], see also [BGBC22] and the references therein.

c) In a certain continuum limit, and with different interpretations of the Lagrange multipliers $\lambda_{1,2}$, (58) can also be derived as the shape equations for carbon nanostructures, see [MDHV13].

d) Besides the Helfrich functional (56), a number of related models exist, for instance the so–called bilayer–coupling (BiC) model [SZ89],

$$E = \int_X H^2 \,\mathrm{d}S, \qquad \text{Lagrangian } F = E + \mu_1(A - A_0) + \mu_2(V - V_0) + \mu_3(M - M_0), \tag{63}$$

where $M = \int_X H \,\mathrm{d}S$ is the integrated mean curvature, $M_0$ is an external parameter, $\mu_{1,2}$ are the Lagrange multipliers for the area and volume constraints, and $\mu_3$ is the Lagrange multiplier for the constraint of fixed area difference between the outer and inner lipid monolayer, expressed via Taylor expansion around a virtual middle layer as $q := M - M_0 = 0$. By identifying $\mu_1 = \lambda + c_0^2$, $\mu_2 = \lambda_2$, and $\mu_3 = -2c_0$, this yields the same shape equation (58) as (57), but the additional constraint $M - M_0 = 0$ drastically changes the phase diagram of minimizers for (63) compared to those for (56). In particular, for (63) closed non–axisymmetric minimizers are known to exist, but not for (56).

Another model is the so called area difference elasticity (ADE) model, where the area difference is not a hard constraint but added as an energy penalization, i.e.,

$$E = \int_X H^2 \,\mathrm{d}S + \frac{\alpha}{2}(M - M_0)^2, \qquad \text{Lagrangian } F = E + \mu_1(A - A_0) + \mu_2(V - V_0), \tag{64}$$

$\alpha > 0$. This again allows stable non–axisymmetric minimizers which moreover compare well to some experimental results; see [WDS96] and [DEK+97], including a discussion of the relations between the

SC, BiC and ADE models.

There are also mechanochemical models which couple bending energies $E=\int_X (H-c_0)^2\,\mathrm{d}S$ with a scalar morphogen on the surface which aggregates in regions of high mean curvature and which in turn increases $c_0$ [MMCRH13], or with for instance Brusselator type reaction–diffusion systems on the surface, where at least one species again increases $c_0$ [TN20]. Most of these models are not variational and somewhat phenomenological, but easily lead to stable non–axisymmetric vesicle shapes, and also to persistent wave–like behavior. However, to the best of our knowledge the (numerical) study of these models so far was restricted to numerical time integration. See also [ES13, BGN15] and the references therein for FEM discretizations of the dynamics of a variety of models, including the SC, the BiC and the ADE models, and, moreover considering the dynamics of vesicles in a fluid. ⌋

From the variety of models related to (56), here we opt for the 'classical' Helfrich SC model, while results including non–axisymmetric minimizers for the BiC model, and some bifurcation study for [MMCRH13] type models will be presented elsewhere.

## 4.1 Vesicles

Following [NT03] we set $\lambda_1 = -\tilde{\lambda}_1/2$ where $\tilde{\lambda}_1$ is the Lagrange multiplier for the area constraint, and write the shape equations (58) as

$$\Delta H + 2H(H^2 - K) + 2c_0K - 2c_0^2H + \lambda_1 H - \lambda_2 = 0, \tag{65a}$$

together with the volume and area constraints

$$q_1(X) = V(X) - V_0 = 0 \quad \text{and} \quad q_2(X) = A(X) - A_0 = 0. \tag{65b}$$

The bending energy $E = \int_X (H-c_0)^2\,\mathrm{d}S$ is scaling $X \mapsto \gamma X$ invariant, and hence a useful dimensionless quantity to characterize solutions of (65) is the reduced volume

$$v = V/V_0, \tag{66}$$

where for given $A = 4\pi R_0^2$ (hence $R_0 = \sqrt{A/4\pi}$), $V_0 = 4\pi R_0/3$ is the volume of the equivalent sphere. At $v = 1$, the sphere is the only solution, and for decreasing $v$ we may expect more and more solutions of various shapes.

**A short review of previous work.** The (wlog unit) sphere is a solution of (65) if (for $N$ the inner normal and hence $H \equiv 1$),

$$\lambda_1 = -2c_0 + 2c_0^2 + \lambda_2. \tag{67}$$

By [NT03, Thm3.1], bifurcations from the sphere occur at

$$\lambda_1 = n(n+1) - 4c_0 + 2c_0^2, \quad \lambda_2 = n(n+1) - 2c_0, \tag{68}$$

$n \geq 2$, with kernels of dimension $2n+1$ spanned by the spherical harmonics $Y_{nm}$, $m = -n, \dots, n$. Already from [Pet83] it is known that branches originating from spherical harmonics with $l \geq 3$ are *never* stable, at least near $v = 1$, while some of the branches bifurcating at the first BP with $n = 2$ contain stable solutions, again see also [NT03]. The bifurcation (unique branch modulo symmetry, see below) is transcritical, with one direction yielding *oblates* (oblate ellipsoids, turning into biconcave RBC shapes, see below for sample plots and more specific classifications), and the other direction yielding *prolates* (prolate ellipsoids). In particular, these are axisymmetric shapes.

An extensive largely numerical study of axisymmetric vesicles is given in [SBL90], including phase and energy diagrams. In a nutshell, the results are [SBL90, Fig.8,10, 11,13,17]:

- In the $v$–$c_0$ phase diagram [SBL90, Fig.10], there is a curve $(0,1] \ni v \mapsto c_0(v)$ decreasing in $v$ and with $c_0(1) = -5/6$ such that near $v = 1$, either oblates (for spontaneous curvature $c_0 < c_0(v)$) or prolates ($c_0 > c_0(v)$) have minimal $E$.
- For decreasing $v$, the prolates lose stability to pears, and the oblates lose stability to stomatocytes. These transitions are discontinuous, i.e., occur via subcritical bifurcations, where the bifurcating branches (pears from prolates, stomatocytes from oblates) gain stability after one (or more) fold(s).
- Some regions in the phase diagram at small $v$ remain unstudied, but in particular for $v > 0.5$, say, there is strong evidence that all local minimizers of $E$ are axially symmetric.

### 4.1.1 Our setup

Given the above results, here we mostly focus on the first BP ($n = 2$ in (68)) and axisymmetric solutions, and only compute a few secondary bifurcations from the axisymmetric branches and some bifurcations from the sphere with $n = 3$. In this, we fix three values of $c_0$, namely $c_0 = 0, c_0 = -1$, and $c_0 = 1.4$, then first continue in $\lambda_1$ along the spherical branch to prepare branch switching at the respective BPs from (68), and after branch–switching to non–spherical solutions continue in $v$, see Remark 4.2. The BDs are then plotted as $E$ over $v$, and agree with [SBL90, Fig.8, 11, 13, 17] for the axisymmetric branches in the $v$–ranges we can reach. Additionally, our stability information is wrt general normal variations, not just axisymmetric ones.

Before we embark on this program we briefly comment on the numerical challenges and solutions to these, see [MU24a] for more (implementation) details. The basic setup again consists in setting $X = X_0 + uN_0$ (with here $N$ the inner normal), and then writing (58) as a system of two second order equations for $(u_1, u_2) = (u, H)$, namely

$$G(u) := \begin{pmatrix} Lu_2 + Mf(u_1, u_2) \\ Mu_2 - H \end{pmatrix} = \begin{pmatrix} 0 \\ 0 \end{pmatrix}. \tag{69}$$

As before, $L$ is the weighted cotangent Laplacian, $M$ the (Voronoi) mass matrix, and

$$f(u_1, u_2) = 2u_2(u_2^2 - K) - 2\lambda_1 u_2 + 2c_0 K - 2c_0^2 u_2.$$

The mean curvature $H{=}H(u_1)$ is computed as $H{=}\frac{1}{2}\langle LX, N\rangle$, and the Gaussian curvature $K{=}K(u_1)$ is obtained from `discrete_curvatures`, cf. (26). The reason for the reformulation of (65a) as two second order equations (69) is that this way we can easily implement the *two* BCs (60) and (61) or (62) when required. See, e.g., [SGJW22] for convergence results on such "mixed FEM" formulations for 4th order problems.

Table 2: Constraints and active parameters for different branch types; the parameters $s_*$ and $r_*$ are the Lagrange multipliers for the translational and rotational constraints, and stay $\mathcal{O}(10^{-6})$ during all continuations.

| type | active parameters | constraints |
|---|---|---|
| trivial (sphere) | $\lambda_1, \lambda_2, s_x, s_y, s_z$ | area $A$ and volume $V$, 3 translational PCs |
| axisymmetric | $v, \lambda_1, \lambda_2, s_x, s_y, s_z, r_1, r_2$ | $A$ and $V$, 3 translational and 2 rotational PCs |
| non–axisymmetric | $v, \lambda_1, \lambda_2, s_x, s_y, s_z, r_1, r_2, r_3$ | $A$ and $V$, 3 translational and 3 rotational PCs |

For closed vesicles, i.e., without any BCs, we always need the three linear translational PCs

$$q_i(X) := \int_{X_0} \langle u, N_i \rangle \, \mathrm{d}X = 0, \quad i = 1, 2, 3, \tag{70}$$

cf. (49), where $N_i$ is the $i$th component of the (here inner) normal $N$ of $X_0$. For (non–spherical) surfaces of revolution (axisymmetric branches), we need two rotational PCs (omitting the axis of revolution). For this, let $\vec{l_1} = (l_1, l_2, l_3)^T$ with $\|\vec{l_1}\| = 1$ be the rotational axis, which we find as

$$\vec{l_1} = X_{i_0} / \|X_{i_0}\| \tag{71}$$

with either $i_0 = \mathrm{argmax}_i \|X_i\|$ (prolates) or $i_0 = \mathrm{argmin}_i \|X_i\|$ (oblates), and take $\vec{l_1}, \vec{l_2}, \vec{l_3}$ with

$$\tilde{l_2} = \begin{pmatrix} -l_2 \\ l_1 \\ 0 \end{pmatrix} + \begin{pmatrix} 0 \\ -l_3 \\ l_2 \end{pmatrix} + \begin{pmatrix} -l_3 \\ 0 \\ l_1 \end{pmatrix}, \quad \vec{l_2} = \frac{\tilde{l_2}}{\|\tilde{l_2}\|}, \text{ and } \vec{l_3} = \vec{l_1} \times \vec{l_2},$$

as an orthonormal basis of $\mathbb{R}^3$. Then the normal variations of rotations around $\vec{l_2}$ and $\vec{l_3}$ are spanned by $\left\langle \vec{l_2} \times X, N \right\rangle$ and $\left\langle \vec{l_3} \times X, N \right\rangle$, and the natural rotational PCs are

$$q_{3+i}(u) := \int_X \left\langle \vec{l_{i+1}} \times X, N \right\rangle u \, \mathrm{d}S = 0, \quad i = 1, 2. \tag{72}$$

For non–axisymmetric $X$ we additionally use the third rotational PC $q_6(u) := \int_X \left\langle \vec{l_1} \times X, N \right\rangle u \, \mathrm{d}S = 0$, and we add $\eta_i \partial_u q_i(u)$ to the first component of $G$ from (69), with Lagrange multipliers $\eta_i$. See Table 2 for a summary. Technically, after branch–switching from the sphere we first do two steps without rotational PCs. For axisymmetric solution branches we then detect the rotational axis via (71) and switch on the two rotational PCs around $\vec{l_2}, \vec{l_3}$. After a secondary bifurcation to a non–axisymmetric branch, or for primary bifurcations to non–axisymmetric branches from the trivial branch ($n \geq 3$ in (68)) we switch on the third rotational PC.

**Remark 4.2** The eigenvalues for the linearization around a steady state are computed from the extended system

$$\begin{pmatrix} M_d & 0 \\ 0 & M_q \end{pmatrix} \partial_t V = - \begin{pmatrix} G_u(U) & G_w(U) \\ q_u(U) & q_w(U) \end{pmatrix} V, \tag{73}$$

where $U = (u, w)$ is the steady state including the active parameters $w$ but without the primary active (genuine continuation) parameter, where $V = (v, z)$ is the perturbation, and where $M_d \in \mathbb{R}^{N \times N}$ and $M_q \in \mathbb{R}^{n_q \times n_q}$ are the pertinent dynamical mass matrices. For (69) we have $N = 2$ and $M_d = \begin{pmatrix} 1 & 0 \\ 0 & 0 \end{pmatrix}$ from the rewriting as a 2nd order system, and $M_q = 0 \in \mathbb{R}^{6 \times 6}$ (axisym. case) or $M_q = 0 \in \mathbb{R}^{7 \times 7}$ (non–axisym. case). Importantly, to obtain the correct stability information we cannot use one of the Lagrange multipliers as primary active parameter, because the Lagrange multipliers are in general not fixed for the flow, and hence we use the reduced volume for the continuation of the nontrivial branches. ⌋

**Remark 4.3** The initial discretization of the sphere is obtained by subdivision and projection (like in Fig.2) with $n_p = 2562$ nodes and $n_t = 5120$ triangles. Many interesting solutions show narrow necks,

and hence adaptive mesh–refinement and coarsening will play a vital role. We set `p.fuha.ufu=@refufu`, where `refufu.m` proceeds in two steps (see also §A.3): First, to deal with small distorted triangles developing at necks we apply a `degcoarsenX`–`refineX` (long)–`retrigX` cycle based on mesh–distortion $\delta_{\rm mesh}$ (element–to–refine–selector `e2rsshape1`). Then we additionally apply `refineX` based on triangle area (selector `e2rsA`) to refine large triangles. As usual, these steps are controlled by switches and tolerances, and suitable choices allow the resolution and robust continuation of rather challenging solutions. However, we also set a soft upper bound of $n_p \le n_{\max} = 5000$ nodes for refinement, i.e., refinement is more strongly controlled when $n_p > n_{\max}$; of course, for axisymmetric solutions a 1D setting as in [SBL90] is more efficient and allows yet finer meshes and hence the resolution of narrower necks. ⌋

### 4.1.2 Results

• $c_0 = 0$**.** Fig.12(a) shows a basic BD for $c_0 = 0$. As already said, we always start with the unit sphere at some $\lambda_1 < 6 - 4c_0 + 2c_0^2$, cf. (68), and initially continue to larger $\lambda_1$ to obtain the BPs from the sphere, although we know them explicitly from (68). This gives the black trivial branch in the 3rd plot in Fig. 12(a). However, for the nontrivial branches we use $v$ as the primary parameter (see Remark 4.2), and get the BD in the first plot in (a), with a zoom in the second.

For the BPs in (68) we have $\lambda_1 = 6$ for $n = 2$ and $\lambda_1 = 12$ for $n = 3$; at the first BP $\lambda_1 = 6$ we have a 5 dimensional kernel of spherical harmonics, but modulo rotations the only bifurcating branch we find bifurcates transcritically in $\lambda_1$ and consists of prolates (orange, stable) in one direction (in $\lambda_1$) and oblates (red, initially unstable) in the other direction, see the samples in (b), with the oblate of the typical RBC shape. The oblates gain stability at $v \approx 0.76$ where the green (non–axisymmetric) branch bifurcates, on which solutions first look like elongated RBCs (pt12) and then become similar to prolates (pt32). The oblates (RBCs) lose stability at $v \approx 0.51$ (and shorty after become non–physical due to self intersections) to a subcritical branch of stomatocytes, which stabilizes in a fold at $v \approx 0.66$, after which solutions at low $v$ take the shape of two spheres, the inner one called an inverted sphere, connected by a narrow neck [SBL90]. We cannot continue the branch below $v = 0.51$ without refining to more than $n_{\max} = 5000$ nodes. Importantly, the stomatocytes have lower $E$ than the oblates for $v \le v_{os} \approx 0.59$, and this corresponds to the discontinuous transition from oblates to stomatocytes in [SBL90, Fig.10].

• $c_0 = -1$**.** For $c_0 = -1 < -5/6$ the first BP is at $\lambda_1 = 12$, and the stabilities of prolates and oblates near $v = 1$ flips, i.e., the oblates are now stable near $v = 1$, and the prolates unstable, and remain so for all $v \in (0, 1)$, see Fig. 13. Near $v = v_s \approx 0.7$ stomatocytes bifurcate subcritically from the oblates, and stabilize in a fold near $v = 0.95$, as in [SBL90, Fig.17]. The red oblates become unphysical near $v = 0.55$ due to self intersections, but the branch folds back near $v = 0.5$ and turns into so–called discocytes with without self–intersections but two invaginations, see o/pt50. According to [SBL90, Fig.17] these discocytes stabilize in a fold near $v \approx 0.85$, but here we cannot continue this branch sufficiently far.

Instead, in Fig.13 we additionally show a "diamond" (tetrahedral symmetry) branch `d` bifurcating from the 2nd BP at $\lambda_1 = 20$, folding back near $v = 0.5$. Subsequently we have four invaginations and at $v \approx 0.72$ we stop the continuation. Moreover, we show the green branch which bifurcates from the first BP on the orange prolates branch. This also folds back, and connects to `d` at $v \approx 0.55$, see panel (c). While all branches shown in (a) are unstable, except the oblates for $v > v_s$, we believe that our selection gives a useful first impression of the extremely rich bifurcation structure, in particular showing that and how 2ndary bifurcations from the $n = 2$ primary branches may connect to $n \ge 3$ branches.

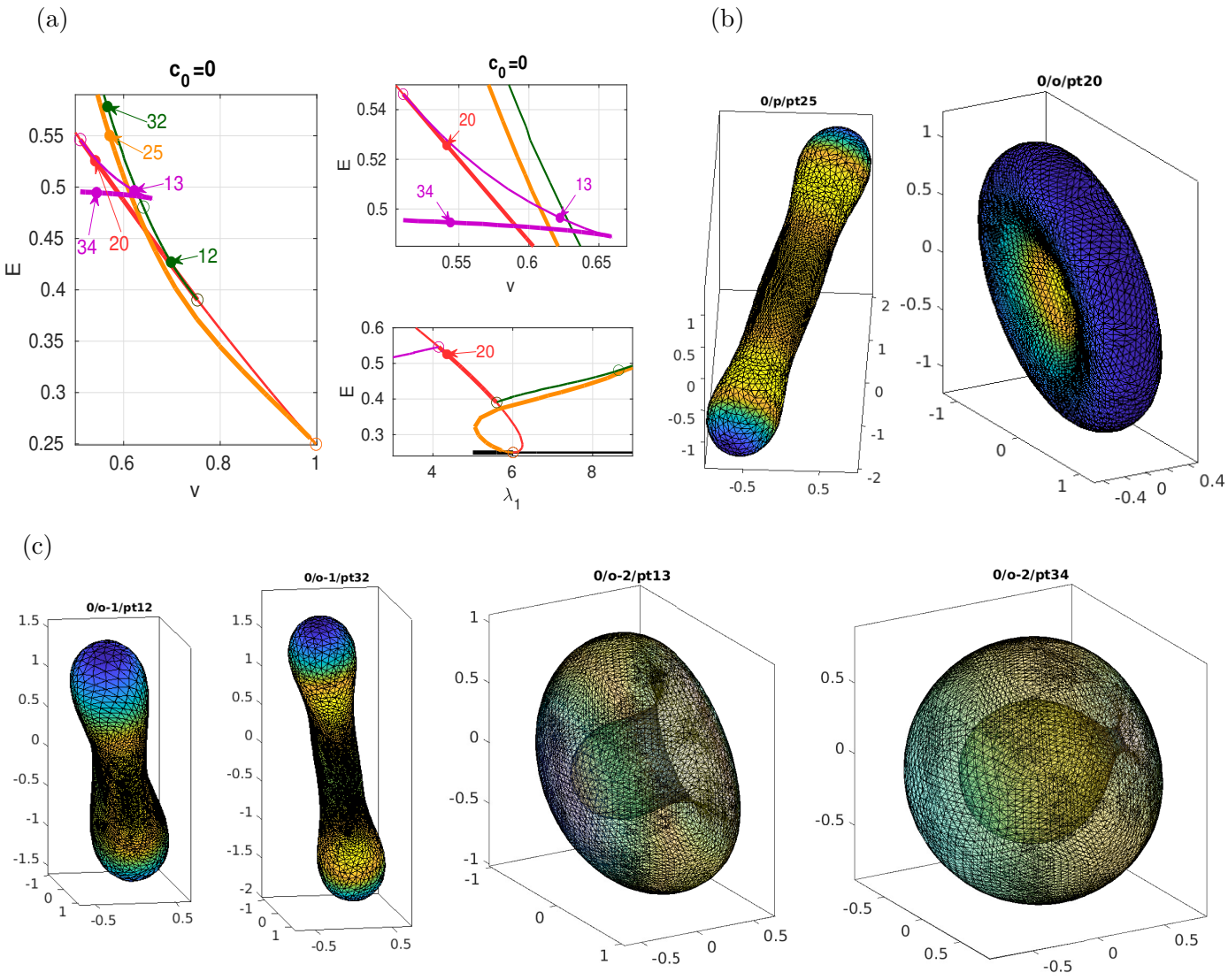


Figure 12: $c_0 = 0$. (a) BDs, $E$ over $v$, with zoom, and $E$ over $\lambda_1$; prolates (orange), oblates (red), and two secondary branches o-1 (green), and o-2 (stomatocytes, violet). (b) samples of one prolate and one oblate. (c) samples along secondary branches bifurcating from oblates.

- $c_0 = 1.4$**.** According to [SBL90, Fig.10], for $c_0 > c_p \approx 1$ and decreasing $v$, oblates lose stability to pears. This is illustrated in Fig.14 for $c_0 = 1.4$, together with some secondary bifurcations from the oblates to D3 and D4 "starfish vesicles" o-1 and o-2, and a tertiary bifurcation to o-1-1a, which can be thought of as an analogue of pears.

In detail, at $v = v_p \approx 0.73$ the green pear branch bifurcates subcritically from the prolates, gains stability in a fold near $v = 0.867$, and shows lower $E$ than the oblates for $v < v_{pp} \approx 0.8$, which hence gives the discontinuous transition from prolates to pears in [SBL90, Fig.10]. Again we remark that the $D_k$ branches with samples in (b) only contain unstable solutions for the SC model. However, some solutions of this type are in fact stable in the BiC model (63), which yields the same Euler–Lagrange equation (58) as (56), but with a different energy $E$ and different constraints, which change the stability properties. Therefore we find it useful to show the branches o-1 and o-2 and associated sample solutions in Fig.14, but a detailed bifurcation analysis of the BiC model will be given elsewhere. Moreover, continuing further the oblate branch we find that the oblates self–intersect for $v < 0.5$ and subsequently there are bifurcations to $D_j$ symmetric self–intersecting starfishes, of which some $D_4$ symmetric ones turn out to be locally stable (but unphysical, and hence not shown).

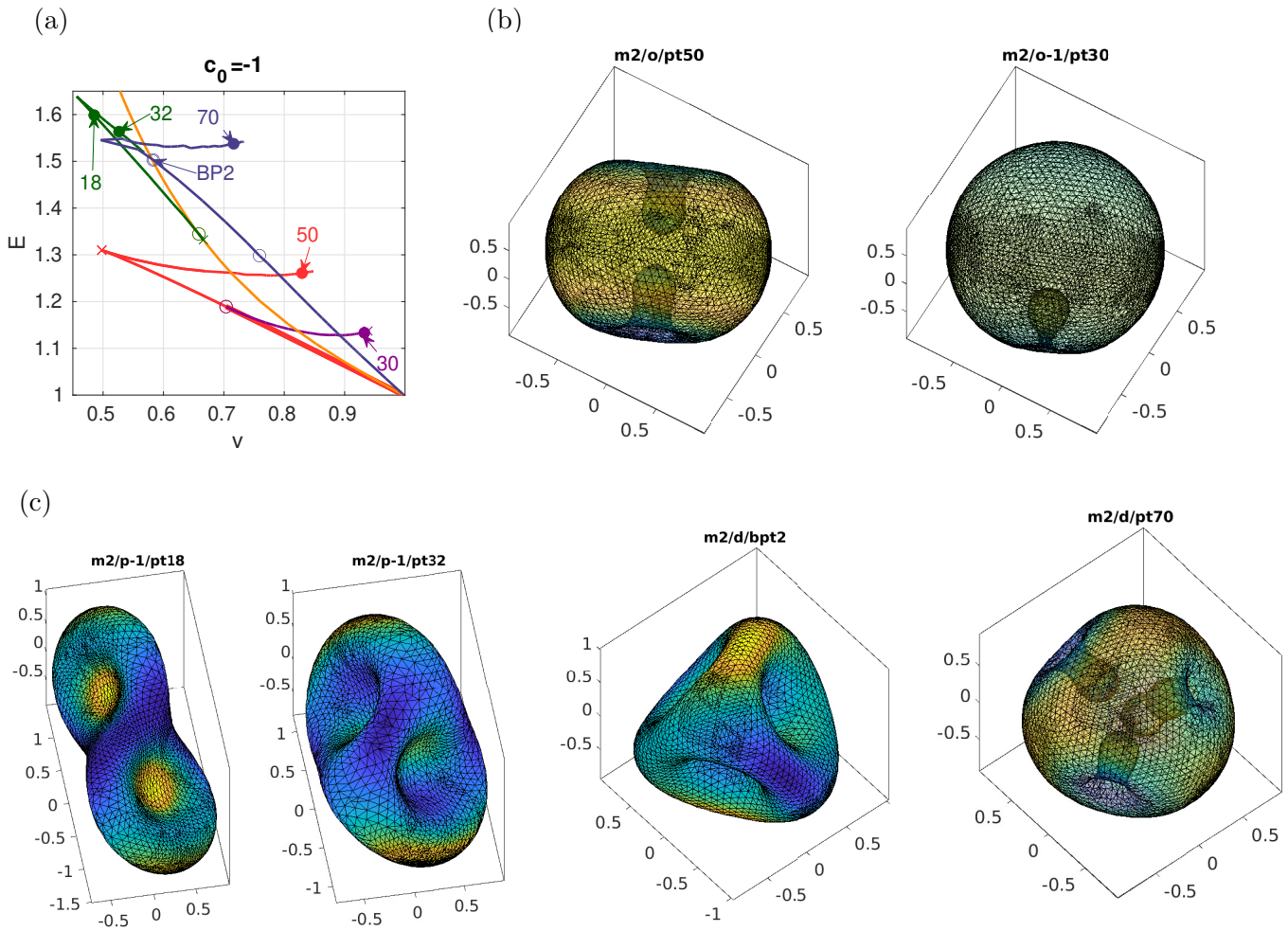


Figure 13: $c_0 = -1$; oblates (red) which turn into discocytes with two stomas; stomatocytes o-1 (violet); prolates (orange), and secondary branch p-1 (green) which connects to (a rotation of) diamonds d (blue) from BP2; the last sample shows the 4 stomas on d.

## 4.2 Biocaps

In the demo `biocaps` we fix the boundary circle $\partial X = \{x^2 + y^2 = \alpha^2\}$ in the $x$–$y$ plane, and additionally require the no-stress BCs (62). Thus,

$$\Delta H + 2H(H^2 - K) + 2c_0 K - 2c_0^2 H - 2\lambda_1 H = 0 \text{ on } X, \text{ and} \tag{74a}$$

$$u = 0 \text{ and } H - c_0 + b\kappa_n = 0 \text{ on } \partial X. \tag{74b}$$

In our experiments we fix $\alpha = 1$ and $\lambda_1 = 1/4$, and first $c_0 = 1/2$ and vary $b$, and want to start with the upper unit hemisphere. Then $H = K = 1$ (choosing the inner normal for the hemisphere) and $\kappa_n = 1$ and hence (74b) requires $b = -1/2$.

**Remark 4.4** a) For $X$ not closed it is an open problem for what parameters, and boundaries and BCs, the minimization of the Lagrangian $F$ from (57) is a well–posed problem. In [Nit93], the following conditions on $c_0, b$ and $\lambda_1$ are posed for $F$ with $\lambda_2 = 0$ to be definite in the sense that $F \geq C_0$ for some $C_0 > -\infty$ for all connected orientable surfaces $X$ of regularity $C^2$ with or without boundary:

$$\text{(i) } \lambda_1 \geq 0, \qquad \text{(ii) } -1 \leq b \leq 0, \qquad \text{and (iii) } -bc_0^2 \leq \lambda_1(1+b). \tag{75}$$

This proceeds as in [Nit91] by scaling properties of $F$ for various surfaces composed of planes (of

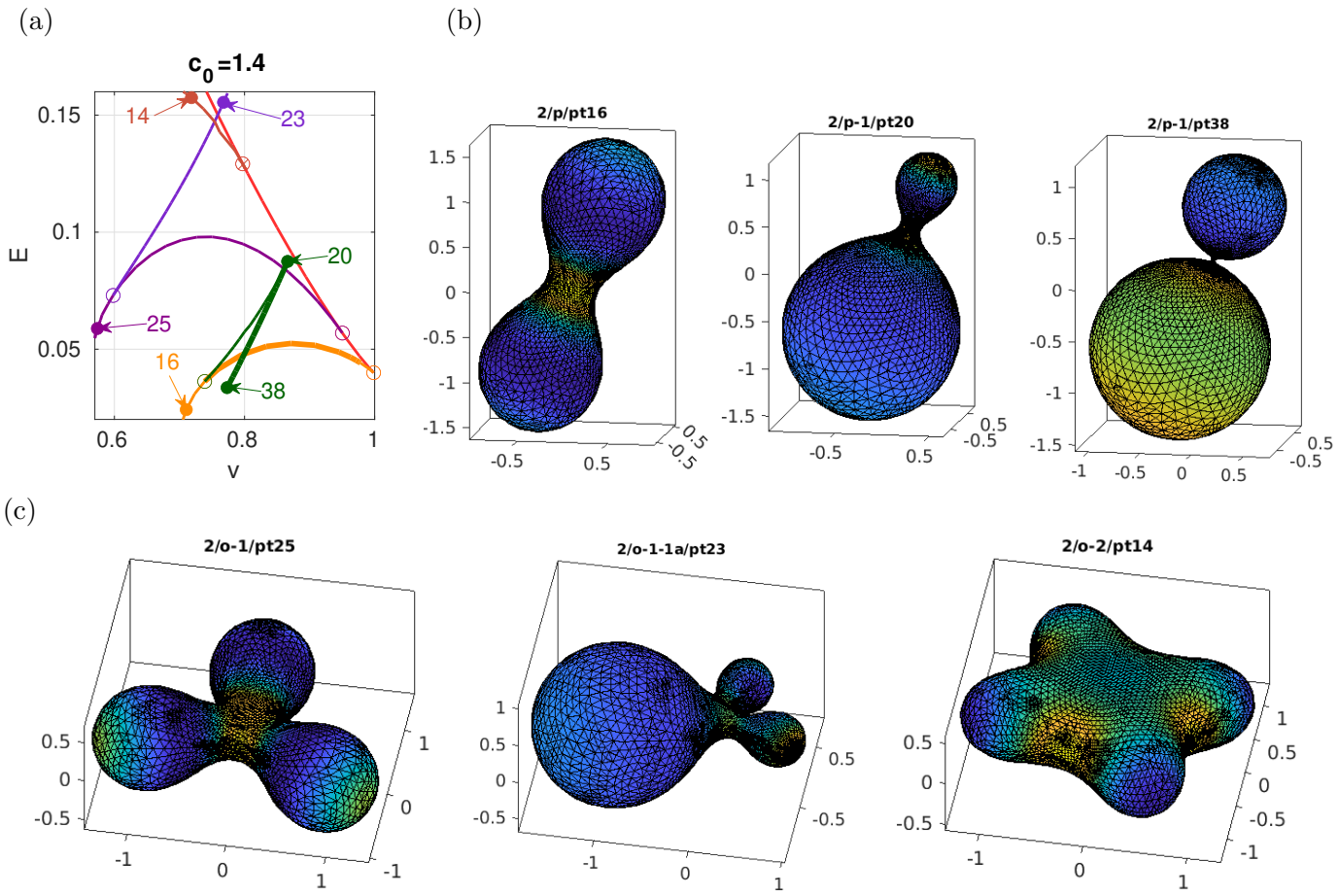


Figure 14: $c_0 = 1.4$. (a) BD, prolates (p, orange), with pears (p-1, green); oblates (red), with secondary bifurcations to D3 (o-1, violet) and D4 (o-2, brown), and tertiary bifurcation (o-1-1a, lilac).

area $A$), cylinders (of lengths $l$ and radius $r_c$), and (hemi)spheres (of radius $r_S$), and considering the asymptotics of $F$ as $A, l \to \infty$ and/or $r_c, r_s \to 0$. For instance, the condition (75)(i) arises most naturally by considering $X$ to contain a plane with $A \to \infty$, which for $\lambda_1 < 0$ gives $L \to -\infty$.

On the other hand, in the physics literature no restrictions on $c_0, b \in \mathbb{R}$ are given, and in a given problem a fixed $\partial X$ and the BCs (61) or (62) may make $F$ definite for much larger ranges than given in (75). In our experiments below we do take parameters to rather extreme values, e.g., $b = -4$ in Fig. 16, where we find interesting solutions, which can then again be continued to moderate parameter regimes.

b) For $\partial X \neq \emptyset$, and in particular for the cases of caps, we are not aware of analytic bifurcation results, except [PP22] which presents some results for caps in a different setting. ⌋

Fig.15(a) shows the continuation of the initial hemisphere in $b$. This is mainly intended for subsequent continuation in $c_0$ at negative $b$, and (b) shows the case of $b \approx -1.66$. The problem is symmetric under $(c_0, X_3) \mapsto -(c_0, X_3)$, and in particular at $c_0 = 0$ we have the flat disk as an exact solution (for any $b$). See `c00b/pt11` for a nearby solution with $c_0 \approx -0.07$, which lies between two folds with exchange of stability. This unstable part will feature interesting bifurcations to non–axisymmetric branches at more negative $b$, see Fig. 16, while the remainder(s) of the axisymmetric branches are all stable, with the samples `c00b/pt34` and `c00/pt14` in 15(b) showing the typical behavior at strongly negative or positive $c_0$, respectively.

**Remark 4.5** The main numerical challenges and used tricks for (74) are:

a) For the initial hemisphere we again use a subdivision and projection algorithm, followed by one mesh–refinement at the boundary, as a good resolution near $\partial X$ turns out helpful later. The

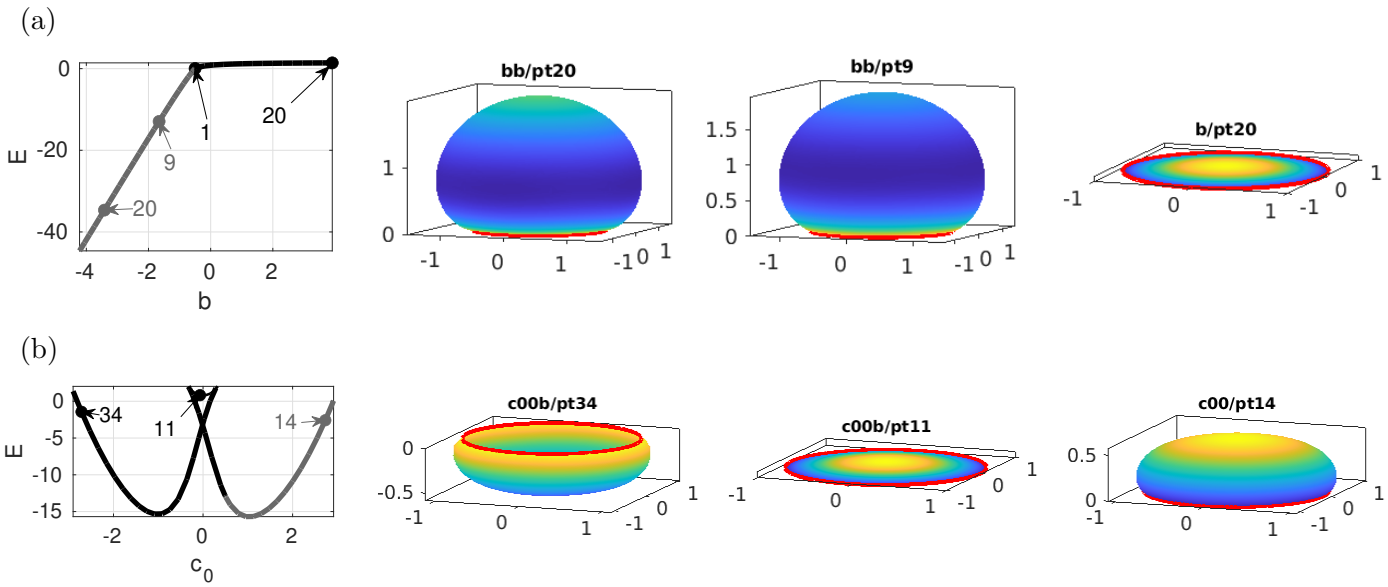


Figure 15: Initial results for (58),(62) from `biocaps/cmds1.m`. In (a) we continue in $b$ starting at `b/pt1` from the unit hemisphere with $(\alpha, \lambda_1, c_0, b) = (1, 1/4, 1/2, -1/2)$, to increasing $b$ (branch `b`, black) and decreasing $b$ (branch `bb`, grey). On `b` we go to the flat disk (last sample), while on `bb` the hemisphere bulges out. This is mainly intended for later continuation in $c_0$, and in (b) we do so starting from `bb/pt9` at $b \approx -1.66$. This gives the double well shape for $E$, with a short unstable segment between the two folds at $c_0 \approx \pm 0.33$. See Fig. 16 for the cases of $b \approx -3.4$ (`bb/pt20`) and $b \approx -4$.

initial mesh then has `np=2245` nodes, which later is refined to `np` $> 6000$. The mesh quality in all our solutions stays quite good, i.e., $\delta_{\text{mesh}} < 20$ for all solutions, and mostly $\delta_{\text{mesh}} < 10$.

b) The boundary $\gamma = \partial X$ is parameterized by arclength as $\gamma(\phi) = \alpha(\cos(\phi/\alpha), \sin(\phi/\alpha), 0)$. Then $\kappa = \gamma'' = -\gamma/\alpha$ and the normal curvature on $\partial X$ reads $\kappa_n = -\frac{1}{\alpha}\langle N, X\rangle$, which is used to implement the BCs (74b).

c) The "integral" `sum(K)` over the discrete Gaussian curvature `K` always evaluates to $2\pi\chi(X)$, cf. Footnote 1. Thus we once more use Gauss-Bonnet $\int_X K \,\mathrm{d}S = 2\pi\chi(X) - \int_{\partial X} \kappa_g \,\mathrm{d}s$ to compute the energy $E$, where $\kappa_g = \text{sign}(N_3)\frac{1}{\alpha}\|N \times \gamma\|$, and where we evaluate $\int_{\partial X} \kappa_g \,\mathrm{d}s$ by a trapezoidal rule. ⌋

In Fig. 16 we repeat the continuation in $c_0$ from Fig. 15(b) at more negative $b$, namely $b \approx -3.4$ in (a,b) and $b \approx -4$ in (c). For lower $b$, the unstable part of the $c_0$ continuation expands, and we find two (or more, for even lower $b$) BPs between the left fold and $c_0$=0, with azimuthal wave numbers $m = 1$ and $m = 2$. As before, these bifurcations are double by $S^1$ symmetry, and to continue the bifurcating branches we set the usual rotational PC after two steps. The blue $m = 1$ branch then behaves similarly in (a) and (b), i.e., it becomes stable after a fold at $c_0 \approx -0.2$ ($b = -3.4$) resp. $c_0 \approx -0.27$ ($b = -4$). However, the $m = 2$ branch behaves differently: For $b = -3.4$ it connects to the symmetric BP at $c_0 > 0$. For $b = -4$, the red branch `c02b-2q` first shows a secondary BP to a branch (`c02b-2q-1`, green) with broken $\mathbb{Z}_2$ symmetry, and then shows a fold at $c_0 \approx -0.21$ where it becomes stable. The branch `c02b-2q-1` also shows a fold, at $c_0 \approx -0.11$, after which however one unstable eigenvalue remains, i.e., $\text{ind}(X) = 1$ at, e.g., `c02b-2q-1/pt20` (last sample in (c)).

Thus we have found *stable* non–axisymmetric solutions, but at rather large $|b|$. In `cmds2.m`, see also [MU24a, Fig.28], we aim to continue the solutions from Fig. 16 to more moderate $|b|$, which however fails due to branches folding back or loosing stability around $b = -3$, and thus the biological significance of the non–axisymmetric solutions from Fig. 16 remains to be discussed.

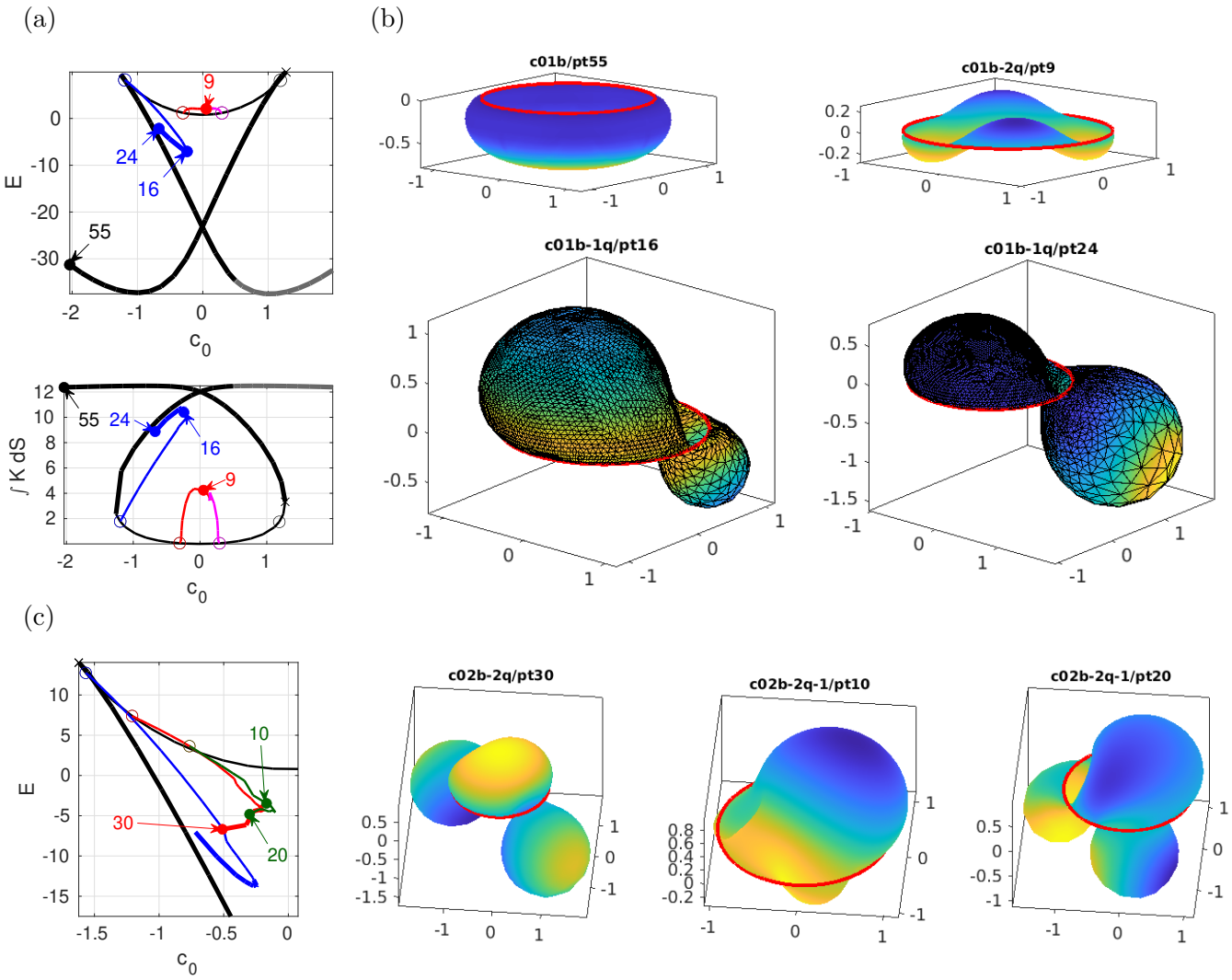


Figure 16: Continuation of Fig. 15. (a,b) Continuation in $c_0$ from `bb/pt20`, $(\alpha, \lambda_1, b) = (1, 0.25, -3.4)$, starting from $c_0 = 0.5$, branches `c01b` (black, to decreasing $c_0$) and `c01` (grey, to increasing $c_0$). There are two BPs on the unstable part of `c01b` for $c_0 < 0$, and the symmetric BPs for $c_0 > 0$. The blue branch `c01b-1q` has azimuthal wave number $m = 1$ and is stable after its fold. The red branch `c01b-2q` has $m = 2$ and connects to the symmetric BP at $c_0 > 0$. The 2nd plot in (a) shows where the part $b \int K \, \mathrm{d}S$ of $E$ becomes dominant, taking into account the rather large $|b|$. (c) Similarly starting at `bb/pt24` with $b \approx -4$; zoom of BD near upper left fold of the branch `c02b` (black) similar to `c01b` from (a). The blue branch is qualitatively as in (a), but now the $m = 2$ branch `c02b-2q` (red) also folds back giving stable solutions, and there is a secondary BP on it, giving the green branch `c02b-2q-1`.

# 5 Summary and outlook

We gave a number of examples for using the `pde2path` extension library `Xcont` for continuation of 2D submanifolds $X$ (surfaces) of $\mathbb{R}^3$. These were partly introductory (the spherical caps in §3.1) and mostly classical, i.e., Enneper's minimal surface in §3.2, the nodoids in §3.3.2, the triply periodic surfaces in §3.4, and the closed vesicles in §4.1, and partly rather specific, i.e., the nodoids with pBCs in §3.3.3, and the biocaps in §4.2. Besides [Bru18], and to some extent [Bra96], there seem to be few numerical continuation and bifurcation experiments for such geometric problems for 2D surfaces, i.e., without imposing some axial symmetry, and we are not aware of a general software for such tasks.

The basic setup for all our problems (except those of 4th order) is similar: We consider CMC surfaces, which mainly differ wrt constraints and/or boundary conditions. Along the way we explained

a number of techniques/tricks which we expect to be crucial in many applications. A major problem for continuation over wider parameter regimes is the mesh handling as $X$ changes, and hence the mesh (strongly) distorts. We explained how this often can be abated via moving of mesh points (`moveX`), refinement (`refineX` which sometimes should be combined with re–triangulation by `retrigX`) and coarsening (`coarsenX`), and coarsening of degenerate triangles (`degcoarsenX`), although the choice of the parameters controlling these functions often requires some trial and error. In any case, $X$ bulging out (increasing area) is usually harmless and can be treated by refinement, but bulging in (the development of necks) requires coarsening and is more challenging.

This is a first step. With the demos we hope to give a pool of applications which users can use as templates for their own problems, and we are curious what other applications users will consider, and of course are happy to help if problems occur. As indicated above, our own further research includes:

- Further classical minimal surfaces (and CMC companions) such as Schwarz H and Scherk surfaces (surface families).
- Alternate models for closed vesicles, which in contrast to the SC model from §4.1 show non–axisymmetric minimizers.
- Coupling of membrane curvature and morphogen dynamics or reaction–diffusion equations as in, e.g., [MMCRH13, TN20], also allowing and showing Hopf bifurcations, as these models are not variational.

# A Appendix

Parts of this have been moved here from the former §3.1, others have been added.

## A.1 The basic numerical continuation and bifurcation algorithms

In its legacy setup, `pde2path` [Uec21b, Uec24] implements numerical continuation and bifurcation for $\ell$–component PDE systems

$$M_d\partial_t u = -G(u,\lambda), \tag{76}$$

where $u : \mathbb{R}\times\Omega \to \mathbb{R}^\ell$, $\Omega\subset\mathbb{R}^d$ a bounded domain, $d = 1, 2, 3$, where $M_d \in \mathbb{R}^{\ell\times\ell}$ is the (dynamical) mass matrix, which may be singular, and where $G$ depends on $u$ and spatial derivatives of $u$, and the parameter (vector) $\lambda \in \mathbb{R}^p$. In the following we identify (76) with its finite dimensional reduction by spatial discretization using for instance the FEM. In many cases we restrict to the steady problem

$$G(u,\lambda) = 0. \tag{77}$$

Often, (77) must be augmented by $n_q \in \mathbb{N}$ additional equations $Q(u,\lambda) = 0 \in \mathbb{R}^{n_q}$, such as phase conditions or, e.g., mass constraints, even if they are automatically fulfilled for the flow of (76) by the choice of initial conditions. However, to simplify the following presentation we now assume $q = 0$, which in principle can always be achieved by appending $Q$ to $G$ and suitable parameters $\widetilde{\lambda}$ to $u$.

**Arclength continuation.** Importantly, *solution branches* of (77) may move back and forth in parameter space (passing through folds), and hence we do not consider them in "natural" parameterization $\lambda \mapsto u(\lambda)$, but in arclength $s \mapsto (u(s),\lambda(s))$ with a (dummy) arclength parameter $s \in \mathbb{R}$. Assuming that after spatial discretization $u \in \mathbb{R}^n$ and that we have one free parameter $\lambda \in \mathbb{R}$, the basic idea is as follows. Given a current solution $(u_n,\lambda_n) \in \mathbb{R}^{n+1}$, and a tangent vector $\tau \in \mathbb{R}^n$ to the already computed part of the branch, we make a predictor $(u^1,\lambda^1) = (u_n,\lambda_n) + \tau$, and solve the

extended system

$$\mathcal{H}(u,\lambda) = \begin{pmatrix} G(u,\lambda) \\ p(u,\lambda,s) \end{pmatrix} = \begin{pmatrix} 0 \\ 0 \end{pmatrix} \in \mathbb{R}^{n+1}, \tag{78}$$

where $p$ is used to make $s$ an approximation of arclength on the branch. The standard choice is

$$p(u,\lambda,s) := \xi \langle u_0', u(s)-u_0 \rangle + (1-\xi)\lambda_0'(\lambda(s)-\lambda_0) - (s-s_0). \tag{79}$$

Here $0 < \xi < 1$ is a weight, typically chosen as $\xi = 1/n$, and $\tau_0$ is assumed to be normalized in the weighted norm

$$\|\tau\|_\xi := \sqrt{\langle \tau, \tau \rangle_\xi}, \qquad \left\langle \begin{pmatrix} u \\ \lambda \end{pmatrix}, \begin{pmatrix} v \\ \mu \end{pmatrix} \right\rangle_\xi := \xi \langle u, v \rangle + (1-\xi)\lambda\mu. \tag{80}$$

For fixed $s$ and $\|\tau_0\|_\xi = 1$, $p(u,\lambda,s) = 0$ thus defines a hyperplane perpendicular (in the inner product $\langle \cdot,\cdot \rangle_\xi$) to $\tau_0$ at distance $\mathrm{ds} := s - s_0$ from $(u_n, \lambda_n)$. Solving (78) (typically by a Newton method) thus means solving (77) on that hyperplane, which in particular allows to go around folds.

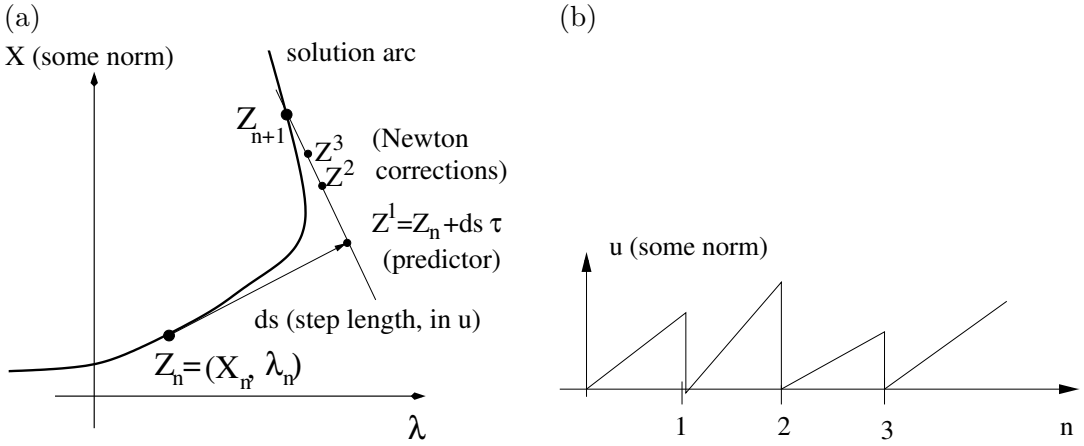


Figure 17: (a) Sketch of arclength continuation algorithm in the `Xcont` setting. (b) Illustration of the "solutions" $u_n$, which are only meaningful together with $X_{n-1}$ via $X_n = X_{n-1} + u_n N_{n-1}$.

This is illustrated in Fig.17, for our `Xcont` setting. Recall that the quantity to compute is $X = X_0 + uN$, which gives the system $G(u,\lambda) = 0$ of type (77) for $u$. The main difference between the `Xcont` setting and the legacy setting of `pde2path` is that for `Xcont` the solution $u_n$ in the $n$th continuation step is only meaningful together with $X_{n-1}$. In particular, after forming the new predictor $Z_n^1$ we initialize the Newton–loop for $u_{n+1}$ with $u_{n+1} = 0$, as illustrated in Fig. 17(b). Nevertheless we keep writing $G(u,\lambda) = 0$ for the defining equation, i.e., do not explicitly display the base manifold $X$ which changes from step to step.

**Bifurcation detection and branch switching.** If $G_u = \partial_u G(u(s_0), \lambda(s_0))$ is invertible at $s_0$, then the implicit function theorem yields that the branch $(s_0-\delta, s_0+\delta) \ni s \mapsto (u(s), \lambda(s))$ is locally unique. Of special interest are singular points where $G_u$ is not invertible and hence other branches may bifurcate. To detect such branch points (BPs), we need suitable test functions.

The simplest case are simple BPs, where exactly one real eigenvalue passes through zero; this can be detected by a sign change of $\det G_u$, which can be efficiently computed from the $LU$–decomposition of $G_u$. However, symmetries often induce higher multiplicities of BPs, and in case of even multiplicity

(and in the case of Hopf–bifurcations, not considered here), $\det G_u$ does not change sign. Thus we provide an alternative method based on inverse vector iteration for computing a few eigenvalues of $G_u$ near 0 (or near a chosen spectral shift, needed for Hopf bifurcations). After detection, BPs should be localized, for instance by a bisection method, although there are much more efficient methods based on suitable extended systems including small eigenvalues, which can also be used to, e.g., continue a BP in a second parameter. All these methods are independent of whether we consider a legacy or `Xcont` problem, and hence we refer to [Uec21b, §3.2–§3.6] for details.

Similarly, the branch switching for `Xcont` problems works as in the legacy setting: for simple BPs we have explicit formulas for the solution of the so called algebraic bifurcation equation for the bifurcation direction $\tau_{\rm bif}$. We set the predictor $X = X_{BP} + \mathrm{d}s\,\tau_{\rm bif} N$ (with normalization $\|\tau_{\rm bif}\|_\xi = 1$), and run a Newton corrector for $u$ to start the continuation of the bifurcating branch. For BPs of higher multiplicity we can numerically derive and solve the pertinent (system of) algebraic bifurcation equations for bifurcation directions $\tau_{\rm bif}^{(1)}, \ldots, \tau_{\rm bif}^{(m)}$, and again use $X^{(j)} = X_{BP} + \mathrm{d}s\,\tau_{\rm bif}^{(j)} N$, $j = 1, \ldots, m$ and solve. Alternatively, and sometimes more robust in practice, we can just compute a base $\phi_1, \ldots, \phi_m$ of $\ker G_u$ and choose $\tau_{\rm bif}$ as linear combination by trial and error; see, e.g., the demo `TPS` and §3.4.2.

## A.2 `pde2path` data structures and functions

Most of the `pde2path` legacy setting [Uec21b, Chapter 5] directly carries over to the `Xcont` setting. Some major changes concern the FEM meshes as explained in §A.3, but so far we summarize:

- All data (FEM-data, solution $u$ and branch tangent $\tau$, active parameter index, tolerances, switches, function handles to define $G, q$, and Jacobians, ...) is kept in a MATLAB struct `p` as in **p**roblem. The main new `Xcont` data is the manifold data in `p.X` and `p.tri`, cf. (20). The most important new switch is

$$\texttt{p.sw.Xcont} = \begin{cases} 0 & \text{legacy setting (no X),} \\ 1 & \text{switch on X–continuation.} \end{cases} \tag{81}$$

  There also is the option `p.sw.Xcont=2` to modify some details of Newton loops, see [MU24a].
- A minimal setup for an `Xcont` continuation (and bifurcation) problem should thus provide an initial `(p.X,p.tri)`, and a function `myG.m` which implements $G$ from (77), linked as in the legacy setup as `p.fuha.sG=@myG`. See also Remark A.1 concerning Jacobians. All demos come with a number of function files, e.g., with * a placeholder for the problem name: `sG*.m` describing the PDE; `*init.m` for initialization. Additionally, there are script files `cmds*.m` with * a number if there is more than one script.
- For backward compatibility, every `Xcont` problem folder must contain a function `M=getM(p)`, which in most cases only contains the line `M=massmatrix(p.X,p.tri,'voronoi')`. In many demos we use customized branch output `out=mybra(p,u)`, to be linked as `p.fuha.outfu=@mybra`. The default is `p.fuha.outfu=@cmcbra`, which writes out the parameter values, $V, A$, and mesh–diagnostics such as $\delta_{\rm mesh}$.
- The discretization of the geometric PDEs is based on the `gptoolbox`, and `pde2path`–interface functions to the `gptoolbox`. There are many convenience functions for standard tasks, see [MU24a] for an overview.
- Since many differential geometric problems (and all our bifurcation demos) come with one or several constraints $q$ (volume, area, phase conditions, ...), there are functions for standard constraints, e.g., `q=qfA(p,u)` and `q=qfV(p,u)` for area/volume constraints, and `qu=qjacA(p,u)` and `qu=qjacV(p,u)` for their derivatives, see also Remark A.1. Importantly, `p.nc.nq` must be set to the number of constraints, and the index vector of active continuation parameters `p.nc.ilam` $= [i_1, i_2, \ldots, i_{n_q+1}]$ must be properly set. Here, $i_1$ is the parameter *index* of the primary

active parameter, and $i_2, \ldots, i_{nq+1}$ are the (indices of) the secondary active parameters.

- The basic `pde2path` commands work as before, e.g.: `p=cont(p,n)` (continue the solution branch – here the branch $s \mapsto (X(s), \lambda(s))$ – for $n$ steps), `p=swibra(dir,pt,newdir)` (attempt branch–switching at a previously computed BP saved in `dir/pt`, with saving of the new branch in `newdir`), `plotbra` (plot a branch into a bifurcation diagram), `plotsol` (plot a solution).

**Remark A.1** An important issue for numerical continuation and bifurcation software for problems of type (3), i.e., $G(u, \lambda) = 0$, is the accurate and efficient computation of Jacobians $\partial_u G$ (and extended Jacobians $\partial_u \begin{pmatrix} G(u) \\ q(u) \end{pmatrix}$, if applicable), which are inter alia needed for Newton loops, computation of branch tangents, bifurcation detection, and branch switching, see §A.1. In general, we recommend to implement a functional form of $\partial_u G$ (linked to `p.fuha.sGjac` and used if `p.sw.jac=1`), and do so in most of our demos. However, for problems with number of mesh points $n_p < 5000$, say, also numerical Jacobians of $G$ are sufficiently fast to not play a role for the speed of the continuation, because MATLAB's `numjac` can efficiently exploit the known sparsity (structure) of $\partial_u G$, in most cases given by the sparsity structure of the Laplacian $L$, or equivalently, by the sparsity structure of the (full, not Voronoi) mass matrix. Thus, for some of our demos, in particular when a functional form of $\partial_u G$ requires major efforts, we content ourselves with numerical Jacobians $\partial_u G$ (and set `p.sw.jac=0`).[13] On the other hand, for typical constraints $q$ such as volume contraints (implemented in the library function `qfV`) we use the functional derivative (implemented in `qjacV`), since $\partial_u q(u) \in \mathbb{R}^{1 \times n_p}$ is dense and numerical derivatives for $\partial_u q$ would be a serious bottleneck. In any case, parameter derivatives such as $\partial_\lambda G$ and $\partial_\lambda q$ are always cheap and thus done numerically. ⌋

## A.3 Meshing

For surface meshes (`X`, `tri`), mesh adaptation is at least as important as for standard (non–parametric) problems, because well behaved initial triangulations (well shaped triangles of roughly equal size) may deteriorate as $X$ changes. The case of uniformly growing parts of $X$, e.g., the growing spherical caps in Fig. 1(a), is rather harmless as triangle sizes grow but shapes stay intact, and can easily be dealt with by refinement of the largest triangles. For this, we simply order the $n_t$ triangles of `tri` by decreasing size, and from these choose the first $\lfloor \sigma n_t \rfloor$ for refinement by `refineX`, i.e., throughout,

$$\sigma = \texttt{p.nc.sig}\text{=parameter for the fraction of triangles to refine.}$$

More generally, the elements–to–refine are linked as `p.fuha.e2rs=@myselector` with a user chosen or provided selector function. For refinement by area the default setting is `p.fuha.e2rs=@e2rsA`. Another option is `p.fuha.e2rs=@e2rsshape1` for refinement by mesh–distortion $\delta_{\text{mesh}} = \max_{\text{triangles}}(h/r)$, cf. (28). The refinement can be either done as RGB, or by refining only the longest edges of the selected triangles, "refine–long" in short. RGB is generally better if triangle shapes are crucial, but may result in rather long cascades to avoid hanging nodes (such that $\sigma$ is only a lower bound for the fraction of triangles actually refined). Refine-long gives more control as *only* the selected triangles are bisected (plus at most one more triangle for each one selected), but may lead to obtuse triangles. A short computation shows that, e.g., for a right–angled triangle refine–long increases $\delta$ by 45%; however, this can often be repaired by combining refine–long with `retrigX`, see below.

Conversely, `coarsenX` can be used to coarsen previously refined triangles, again from a list generated by some criterion, e.g., the $\lfloor \sigma n_t \rfloor$ triangles of *smallest* area, but these have to be from the list of previously refined triangles.

[13] For testing implementations there is the function `jaccheck(p)` and as a rule of thump the relative error between the user Jacobian and the `numjac` Jacobian should not exceed $10^{-6}$.

`degcoarsenX` works differently: It aims to collapse short edges to remove acute triangles, defined by $s-r > 2R$, where $s, r, R$ are the semiperimeter, the inradius, and the circumradius for each triangle. For us, this is mainly important for *small* acute triangles (which develop when $X$ bulges in, i.e., at necks), and hence before coarsening we compute a size parameter $\varepsilon = |T_{n_c}|$ where we assume the triangles ordered by increasing size and let $n_c = \lfloor \sigma_c n_t \rfloor$, with $\sigma_c =$ `p.nc.sigc` a user chosen fraction (upper bound) of triangles to coarse. Then, only acute triangles of size $|T| \leq \varepsilon$ are coarsened. Both, `refineX` and `degcoarsenX` can be told to *not* refine/coarsen boundary triangles, which is useful for the case of periodic BCs.

We also provide two small modifications of (actually interfaces to) code from [PS04]. In `retrigX.m` we generate a new (Delauney) triangulation of $X$, keeping intact the surface structure of $X$. This is in particular useful if $X$ has been obtained from *long* refinement, which typically results in nodes having 8 adjacent triangles (valence 8), while "standard" triangulations (and, for most nodes, the output of `retrigX`) have valence 5 and 6, which generally results in more robust continuations. In `moveX` we combine `retrigX` with motion of the points in $X$ due to "truss forces" of the triangulation, aimed at more uniform edge lengths. Due to the similarity of the triangulation truss forces and surface tension, this works best for minimal surfaces ($H$=0), or otherwise for surfaces with small $|H|$.

In `refineX, coarsenX`, and `degcoarsenX`, the last solution $u$ and in particular the $u$ component of the branch tangent $\tau$ are interpolated to the new $X$, but the PDE $G(u, \lambda) = 0$ is *not* directly solved to correct the refinement/coarsening/interpolation error. In simple cases, if any of the above functions is called during continuation, for instance in a "REFinement–User–FUnctions" `refufu.m`, the next solution step is done in the next continuation step; see `refufu.m` and `refufumaxA.m` in the demo `spcap1`, §3.1. In more complicated cases, e.g., when more than one of `refineX, coarsenX`, and `degcoarsenX` are called for adaptation, it may be advantageous to solve $G(u, \lambda) = 0$ for correction between the different calls; see `refufu.m` in the demo `vesicles`, §4.1. The same applies in principle to `retrigX` and `moveX`, which keep the number of mesh–points fixed but deliberately change the (discrete) system $G(u, \lambda) = 0$. However, in our demos we always call `retrigX` and `moveX` in direct combination with one of `refineX, coarsenX` or `degcoarsenX`, and hence the error introduced by `retrigX` and `moveX` is taken care of automatically by the subsequent solve.

**Example A.2** As an example for different meshing and mesh refinement options, in the demo `parabol` we consider the (non–parametric) quarter of a paraboloid

$$P = \{z = z_a(x, y) : (x, y) \in Q = (0, 1)^2\}, \text{ where } z_a(x, y) = x^2/a^2 + y^2/b^2.$$

The mean curvature of $P$ is $H_P(x, y) = \dfrac{a^2 + b^2 + 4x^2/a^2 + 4y^2/b^2}{a^2 b^2 (1 + 4x^2/a^4 + 4y^2/b^4)^{3/2}}$, and hence we want to solve for $X$ the Dirichlet problem

$$H - H_P = 0, \quad z = z_a \text{ for } (x, y) \in \partial Q. \tag{82}$$

We start with a coarse initial mesh ($n_p$=36 points) in the $x$–$y$–plane, mapped to $\mathbb{R}^3$ as $(x, y, z_a(x, y))$. This is *not* a solution of the discrete problem (82) due to the discretization error of the numerical $H$ (see Fig.2 and Fig.3). Hence we want to solve (82) and use mesh adaptation to improve the approximation, which we measure as $z - z_a$ (in different norms). In Fig. 18(a–c) we first show three options for meshes. In (a), we have a default triangle mesh in the $x$–$y$ plane, while (b) shows a "criss–cross" mesh obtained from (a) by one uniform "refine–long" step. In contrast to (a), (b) is symmetric (in the $x$–$y$ plane) wrt reflection in $x$ and $y$, and such meshes have proven useful for legacy PDE problems in the plane (and in 3D), where it is sometimes crucial to have the mesh reflect symmetries of the

PDE, see [Uec21b, §4.1.1]. From the `Xcont` point–of–view, a salient feature of (b) is that it alternates valence 4 and valence 8 points in the bulk, which always happens when applying refine-long to a valence–6–triangle mesh. In (c) we have the same points as in (b) but applied `retrigX`, which here converted most of the bulk nodes back to valence 6.

We now use the mesh from (a) and three different iterative "adaption-solve" strategies $S_j$, $j = 0, 1, 2$ to approximate the known solution $(x, y, z_a(x, y))$ of (82). In $S_0$ we use $M_{\text{full}}$ and refine-long of the $\sigma = 1/2$ largest triangles. $S_1$ is like $S_0$ but with $M = M_{\text{Voronoi}}$ instead of $M_{\text{full}}$, and $S_2$ is $S_1$ but with `retrigX` after each refinement. In (d,e) we show the errors for $S_0$ and $S_2$ after one step ($S_1$ is quite similar to $S_0$ here), with refinement in the $y \geq 1/2$ part of the initial mesh due to the larger triangles there from the mapping of the initial uniform planar mesh to 3D via $z = z_a(x, y)$. The main message is that the main error sits at the valence 4 and 5 nodes, and that refine–long followed by `retrigX` introduces a layer of valence 5 nodes between parts that have/have not been refined. As shown in (f), $S_2$ is best for the given simple problem, but the overall convergence (in $\|\cdot\|_\infty$) of the three strategies is similar, and we have also have the same rate $\approx -1$ in $\|\cdot\|_2$. ⌋

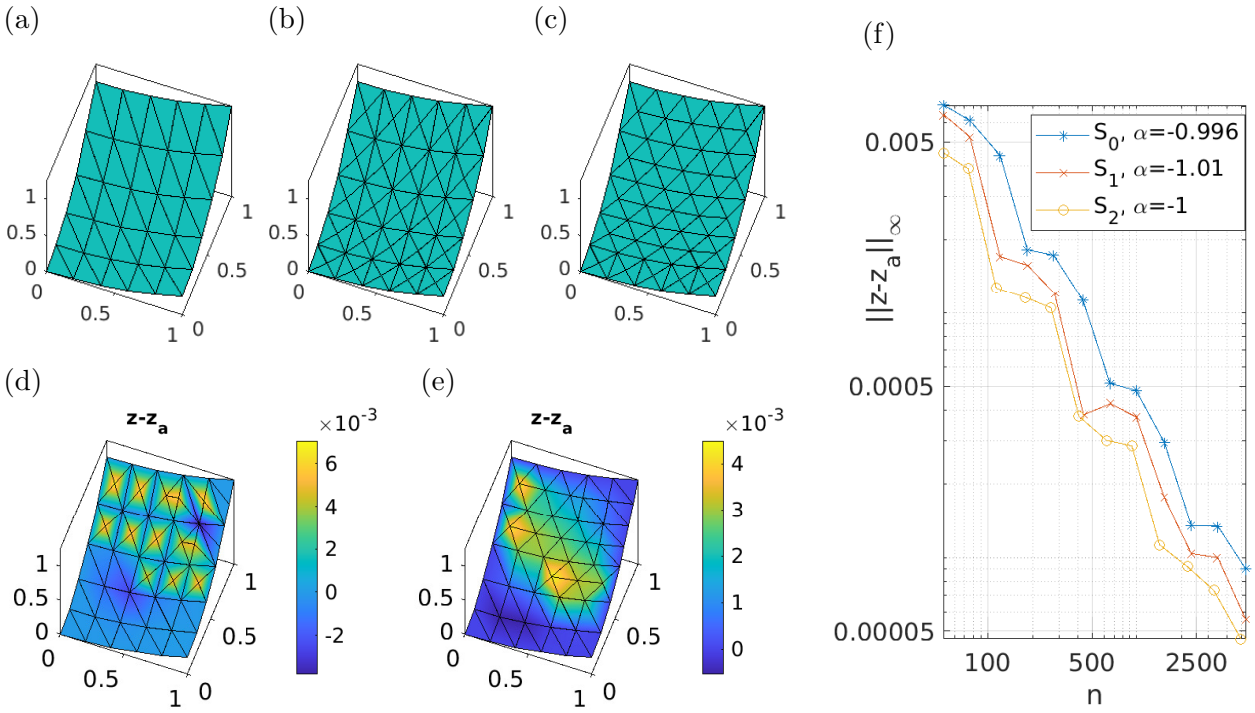


Figure 18: Example A.2, `geomtut/parabol/cmds1.m`. Initial mesh (a), different mesh–refiments and local effects on error (b)–(e), but similar overall convergence (f).

# References


[AHLL88] S Andersson, S. T. Hyde, K Larsson, and S. Lidin. Minimal surfaces and structures: from inorganic and metal crystals to cell membranes and biopolymers. *Chemical Reviews*, 88(1):221–242, 1988.

[ALP99] L. J. Alías, R. López, and B. Palmer. Stable constant mean curvature surfaces with circular boundary. *Proc. Amer. Math. Soc.*, 127(4):1195–1200, 1999.

[BF67] R. Bowen and St. Fisk. Generations of triangulations of the sphere. *Mathematics of Computation*, 21:250–252, 1967.

[BGBC22] M. Bottacchiari, M. Gallo, M. Bussoletti, and C. Casciola. Activation energy and force fields during topological transitions of fluid lipid vesicles. *Commun. Phys.*, 5:12, 2022.

[BGN15] J. Barrett, H. Garcke, and R. Nürnberg. Numerical computations of the dynamics of fluidic membranes and vesicles. *PRE*, 92:052704, 2015.

[BGN20] J. Barrett, H. Garcke, and R. Nürnberg. Parametric finite element approximations of curvature-driven interface evolutions. In *Geometric partial differential equations. Part I*, volume 21 of *Handb. Numer. Anal.*, pages 275–423. Elsevier, Amsterdam, 2020.

[BGNZ22] Weizhu Bao, H. Garcke, R. Nürnberg, and Quan Zhao. Volume-preserving parametric finite element methods for axisymmetric geometric evolution equations. *J. Comput. Phys.*, 460:Paper No. 111180, 23, 2022.

[BNP10] A. Bonito, R. H. Nochetto, and M. S. Pauletti. Geometrically consistent mesh modification. *SIAM J. Numer. Anal.*, 48(5):1877–1899, 2010.

[Bra92] K. Brakke. The surface evolver. *Experiment.Math.*, 1(2):141–165, 1992.

[Bra96] K. Brakke. The surface evolver and the stability of liquid surfaces. *Philos. Trans. Roy. Soc. London Ser. A*, 354(1715):2143–2157, 1996.

[Bra23] K. Brakke. Triply Periodic Minimal Surfaces, 2023. `http://facstaff.susqu.edu/brakke/evolver/examples/periodic/periodic.html`.

[Bru18] N. D. Brubaker. A continuation method for computing constant mean curvature surfaces with boundary. *SIAM J. Sci. Comput.*, 40(4):A2568–A2583, 2018.

[BT84] M. J. Beeson and A. J. Tromba. The cusp catastrophe of Thom in the bifurcation of minimal surfaces. *Manuscripta Math.*, 46(1-3):273–308, 1984.

[CK97] T. K. Callahan and E. Knobloch. Symmetry-breaking bifurcations on cubic lattices. *Nonlinearity*, 10:1179–1216, 1997.

[CR71] M. G. Crandall and P. H. Rabinowitz. Bifurcation from simple eigenvalues. *J. Functional Analysis*, 8:321–340, 1971.

[DCF+97] E. Doedel, A. R. Champneys, T. F. Fairgrieve, Y. A. Kuznetsov, B. Sandstede, and X. Wang. AUTO: Continuation and bifurcation software for ordinary differential equations (with HomCont). `http://indy.cs.concordia.ca/auto/`, 1997.

[DE13] G. Dziuk and Ch. M. Elliott. Finite element methods for surface PDEs. *Acta Numer.*, 22:289–396, 2013.

[DEK+97] H.-G. Döbereiner, E. Evans, M. Kraus, U. Seifert, and M. Wortis. Mapping vesicle shapes into phase diagrams: A comparison of experiment and theory. *PRE*, 55(4):4485–4474, 1997.

[Des04] M. Deserno. Notes on differential geometry, `https://www.cmu.edu/biolphys/deserno/pdf/diff_geom.pdf`, 2004.

[DLW06] Qiang Du, Chun Liu, and Xiaoqiang Wang. Simulating the deformation of vesicle membranes under elastic bending energy in three dimensions. *J. Comput. Phys.*, 212(2):757–777, 2006.

[DS13] H. Dankowicz and F. Schilder. *Recipes for continuation*, volume 11 of *Comp. Sc. & Eng.* SIAM, Philadelphia, PA, 2013.

[ES13] C. M. Elliott and B. Stinner. Computation of two-phase biomembranes with phase dependent material parameters using surface finite elements. *Commun. Comput. Phys.*, 13(2):325–360, 2013.

[ES18] Norio Ejiri and Toshihiro Shoda. The Morse index of a triply periodic minimal surface. *Differential Geometry and its Applications*, 58:177–201, 2018.

[FVKG22] B. Foster, N. Verschueren, E. Knobloch, and L. Gordillo. Pressure-driven wrinkling of soft inner-lined tubes. *New J. Phys.*, 24(January):Paper No. 013026, 15, 2022.

[FW14] S. Fujimori and M. Weber. A contruction method for triply periodic minimal surfaces. In *Proceedings of the 16th OCU*, pages 79–90. OCAMI Studies, 2014.

[GBMK01] P. J. F. Gandy, S. Bardhan, A. L. Mackay, and J. Klinowski. Nodal surface approximations to the P,G,D and I-WP triply periodic minimal surfaces. *Chemical Physics Letters*, 336:187–195, 2001.

[GK00] P. J. F. Gandy and J. Klinowski. Exact computation of the triply periodic Schwarz P minimal surface. *Chemical Physics Letters*, 322:579–586, 2000.

[GS02] M. Golubitsky and I. Stewart. *The symmetry perspective*. Birkhäuser, Basel, 2002.

[Har13] D. Hartley. Motion by volume preserving mean curvature flow near cylinders. *Comm. Anal. Geom.*, 21(5):873–889, 2013.

[Hel73] W. Helfrich. Elastic properties of lipid bilayers: Theory and possible experiments. *Zeitschrift für Naturforschung*, 28:693, 1973.

[Hof90] D. A. Hoffman. Some basic facts, old and new, about triply periodic embedded minimal surfaces. *J. Physique*, 51:197–208, 1990. Intern. Workshop on Geometry and Interfaces (Aussois, 1990).

[Hoy06] R.B. Hoyle. *Pattern formation*. Cambridge University Press., 2006.

[Jac13] A. Jacobson. Algorithms and interfaces for real- time deformation of 2D and 3D shapes, `https://doi.org/10.3929/ethz-a-00979066`, 2013.

[Jac24] A. Jacobson. gptoolbox, `https://github.com/alecjacobson/gptoolbox`, 2024.

[JQJZC98] Yan Jie, Liu Quanhui, Liu Jixing, and Ou-Yang Zhong-Can. Numerical observation of nonaxisymmetric vesicles in fluid membranes. *Phys. Rev. E*, 58:4:4730–4736, 1998.

[Kie12] H. Kielhöfer. *Bifurcation theory*. Springer, New York, second edition, 2012. An introduction with applications to partial differential equations.

[KIPM+20] V. Kralj-Iglc, G. Pocsfalvi, L. Mesarec, V. Šuštar, H. Hägerstrand, and A. Iglic. Minimizing isotropic and deviatoric membrane energy–an unifying formation mechanism of different cellular membrane nanovesicle types. *PLOS ONE*, 2020.

[KN06] Y. Kohsaka and T. Nagasawa. On the existence of solutions of the Helfrich flow and its center manifold near spheres. *Differential Integral Equations*, 19(2):121–142, 2006.

[KPP15] M. Koiso, B. Palmer, and P. Piccione. Bifurcation and symmetry breaking of nodoids with fixed boundary. *Adv. Calc. Var.*, 8(4):337–370, 2015.

[KPP17] M. Koiso, B. Palmer, and P. Piccione. Stability and bifurcation for surfaces with constant mean curvature. *Journal of the Mathematical Society of Japan*, 69(4):1519 – 1554, 2017.

[KPS18] M. Koiso, P. Piccione, and T. Shoda. On bifurcation and local rigidity of triply periodic minimal surfaces in $\mathbb{R}^3$. *Ann. Inst. Fourier (Grenoble)*, 68(6):2743–2778, 2018.

[Lóp13] R. López. *Constant Mean Curvature Surfaces with Boundary*. Springer, 2013.

[LWM08] G. Lim, M. Wortis, and R. Mukhopadhyay. Red blood cell shapes and shape transformations: Newtonian mechanics of a composite membrane. In *Soft Matter: Lipid Bilayers and Red Blood Cells, Volume 4*, pages 83–254, 2008.

[Man11] C. Mantegazza. *Lecture notes on mean curvature flow*. Birkhäuser/Springer Basel, 2011.

[MDHV13] I. M Mladenov, P. A. Djondjorov, M. T. Hadzhilarova, and V. M. .Vassilev. Equilibrium configurations of lipid bilayer membranes and carbon nanostructures. *Comm. Theor. Phys.*, 59(2):213–228, 2013.

[MDSB03] M. Meyer, M. Desbrun, P. Schröder, and A. H. Barr. Discrete differential-geometry operators for triangulated 2-manifolds. In *Visualization and mathematics III*, Math. Vis., pages 35–57. Springer, Berlin, 2003.

[MMCRH13] M. Mercker, A. Marciniak-Czochra, T. Richter, and D. Hartmann. Modeling and computing of deformation dynamics of inhomogeneous biological surfaces. *SIAM J. Appl. Math.*, 73(5):1768–1792, 2013.

[MP02] R. Mazzeo and Fr. Pacard. Bifurcating nodoids. In *Topology and geometry: commemorating SISTAG*, volume 314 of *Contemp. Math.*, pages 169–186. AMS, Providence, RI, 2002.

[MU24a] A. Meiners and H. Uecker. Differential geometric bifurcation problems in `pde2path` – algorithms and tutorial examples, 2024. Available at [Uec24].

[MU24b] A. Meiners and H. Uecker. Supplementary information for *Differential geometric bifurcation problems in* `pde2path`, `www.staff.uni-oldenburg.de/hannes.uecker/pde2path/tuts`, 2024.

[Nit76] J. C. C. Nitsche. Non-uniqueness for Plateau's problem. A bifurcation process. *Ann. Acad. Sci. Fenn. Ser. A I Math.*, 2, 1976.

[Nit91] J. C. C. Nitsche. Periodic surfaces which are extremal for energy functionals containing curvature functions. IMA Preprint Series #785, 1991.

[Nit93] J. C. C. Nitsche. Boundary value problems for variational integrals involving surface curvatures. *Quart. Appl. Math.*, 51(2):363–387, 1993.

[NT03] T. Nagasawa and I. Takagi. Bifurcating critical points of bending energy under constraints related to the shape of red blood cells. *Calc. Var. PDEs*, 16(1):63–111, 2003.

[Oss14] R. Osserman. *A Survey of Minimal Surfaces*. Dover reprint of the 1968 edition, 2014.

[OYT14] Z. C. Ou-Yang and Z. C. Tu. Overview of the study of complex shapes of fluid membranes, the Helfrich model and new applications. In *Proceedings of the conference in honour of the 90th birthday of Freeman Dyson*, pages 277–287. World Sci. Publ., Hackensack, NJ, 2014.

[Pet83] Mark A. Peterson. An instability of the red blood cell shape. *Journal of Applied Physics*, 57:1739–1742, 1983.

[Pla73] J. Plateau. *Experimental and theoretical statics of liquids subject to molecular forces only*, translated by K. Brakke, `facstaff.susqu.edu/brakke/plateaubook/plateaubook.html`, 1873.

[PP22] B. Palmer and Á. Pámpano. The Euler-Helfrich functional. *Calc. Var. Partial Differential Equations*, 61(3):Paper No. 79, 28, 2022.

[PS04] P. Persson and G. Strang. A simple mesh generator in matlab. *SIAM Review*, 46(2):329–345, 2004.

[Ros92] M. Ross. Schwarz' $P$ and $D$ surfaces are stable. *Differential Geom. Appl.*, 2(2):179–195, 1992.

[Ros05] W. Rossman. The first bifurcation point for Delaunay nodoids. *Experiment. Math.*, 14(3):331–342, 2005.

[Ruc81] H. Ruchert. A uniqueness result for Enneper's minimal surface. *Indiana Univ. Math. J.*, 30(3):427–431, 1981.

[SAR97] L. Slobozhanin, J. Alexander, and A. Resnick. Bifurcation of the equilibrium states of a weightless liquid bridge. *Phys. Fluids*, 9(7):1893–1905, 1997.

[SBL90] U. Seifert, K. Berndl, and R. Lipowsky. Shape transformations of vesicles: Phase diagram. *PRA*, 44:1182–1202, 1990.

[Sei97] U. Seifert. Configurations of fluid membranes and vesicles. *Advances in Physics*, 46(1):13–137, 1997.

[SGJW22] O. Stein, E. Grinspun, A. Jacobson, and M. Wardetzky. A mixed finite element method with piecewise linear elements for the biharmonic equation on surfaces, `http://arxiv.org/pdf/1911.08029`, 2022.

[She02] J. R. Shewchuk. What is a good linear element? Interpolation, conditioning, and quality measures. In *Eleventh International Meshing Roundtable (Ithaca, New York)*, pages 115–126, 2002.

[SL95] U. Seifert and R. Lipowsky. Morphology of Vesicles. In R.Lipowsky and E. Sackmann, editors, *Handbook of Biological Physics*, volume 1, pages 403–463. Elsevier, 1995.

[STFH06] G. E. Schröder-Turk, A. Fogden, and S. T. Hyde. Bicontinuous geometries and molecular self-assembly: comparison of local curvature and global packing variations in genus-three cubic, tetragonal and rhombohedral surfaces. *Europ.Phys.J.B - Condensed Matter and Complex Systems*, 54(4):509–524, 2006.

[SZ89] S. Svetina and B. Zeks. Membrane bending energy and shape determination of phospholipid vesicles and red blood cells. *Eur.Biophys J,*, 17(2):101–111, 1989.

[Tap16] K. Tapp. *Differential geometry of curves and surfaces*. Springer, [Cham], 2016.

[TN20] Naoki Tamemoto and Hiroshi Noguchi. Pattern formation in reaction–diffusion system on membrane with mechanochemical feedback. *Scientific reports*, 10(19582), 2020.

[Uec21a] H. Uecker. Continuation and bifurcation for Nonlinear PDEs – algorithms, applications, and experiments. *Jahresbericht DMV*, 2021.

[Uec21b] H. Uecker. *Numerical continuation and bifurcation in Nonlinear PDEs*. SIAM, Philadelphia, PA, 2021.

[Uec24] H. Uecker. `www.staff.uni-oldenburg.de/hannes.uecker/pde2path`, 2024.

[UWR14] H. Uecker, D. Wetzel, and J.D.M. Rademacher. pde2path – a Matlab package for continuation and bifurcation in 2D elliptic systems. *NMTMA*, 7:58–106, 2014.

[UY17] Masaaki Umehara and Kotaro Yamada. *Differential geometry of curves and surfaces*. World Scientific, 2017. Translated from the second (2015) Japanese edition by W.Rossman.

[VDM08] V. M. Vassilev, P. A. Djondjorov, and I. M. Mladenov. Cylindrical equilibrium shapes of fluid membranes. *J. Phys. A*, 41(43):435201, 16, 2008.

[Vel20] R. Veltz. BifurcationKit.jl, `https://hal.archives-ouvertes.fr/hal-02902346`, 2020.

[War08] M. Wardetzky. Convergence of the cotangent formula: an overview. In *Discrete differential geometry*, volume 38 of *Oberwolfach Semin.*, pages 275–286. Birkhäuser, Basel, 2008.

[WBD97] A. De Wit, P. Borckmans, and G. Dewel. Twist grain boundaries in 3D lamellar Turing structures. *Proc. Nat. Acad. Sci.*, 94:12765–12768, 1997.

[WDS96] W. Wintz, H.-G. Döbereiner, and U. Seifert. Starfish vesicles. *EPL*, 33(5):403–408, 1996.

[Xu04] Guoliang Xu. Convergent discrete Laplace–Beltrami operators over triangular surfaces. *Computer Aided Geometric Design*, 21:767–784, 2004.

[XX09] Zhiqiang Xu and Guoliang Xu. Discrete schemes for Gaussian curvature and their convergence. *Comput. Math. Appl.*, 57(7):1187–1195, 2009.